

Serveur Académique Lausannois SERVAL serval.unil.ch

Author Manuscript

Faculty of Biology and Medicine Publication

This paper has been peer-reviewed but does not include the final publisher proof-corrections or journal pagination.

Published in final edited form as:

Title: Autosis is a Na⁺,K⁺-ATPase-regulated form of cell death triggered by autophagy-inducing peptides, starvation, and hypoxia-ischemia.

Authors: Liu Y, Shoji-Kawata S, Sumpter RM Jr, Wei Y, Ginet V, Zhang L, Posner B, Tran KA, Green DR, Xavier RJ, Shaw SY, Clarke PG, Puyal J, Levine B

Journal: Proceedings of the National Academy of Sciences of the United States of America

Year: 2013 Dec 17

Volume: 110

Issue: 51

Pages: 20364-71

DOI: 10.1073/pnas.1319661110

In the absence of a copyright statement, users should assume that standard copyright protection applies, unless the article contains an explicit statement to the contrary. In case of doubt, contact the journal publisher to verify the copyright status of an article.

Autosis, a Na⁺,K⁺-ATPase-Regulated Form of Autophagic Cell Death

Triggered by Autophagy-Inducing Peptides, Starvation and Hypoxia-Ischemia

Yang Liu^{1,2}, Sanae Shoji-Kawata^{1,2*}, Rhea Sumpter^{1,2}, Yongjie Wei^{1,2,5}, Vanessa Ginet⁶,
Liyang Zhang³, Bruce Posner³, Khoa A. Tran⁷, Douglas R. Green¹¹, Ramnik Xavier^{8,9,10},
Stanley Y. Shaw^{7,10}, Peter G.H. Clarke⁶, Julien Puyal^{6#}, and Beth Levine^{1,2,4,5#}

Center for Autophagy Research¹, Department of Internal Medicine², Department of Biochemistry³, Department of Microbiology⁴, and Howard Hughes Medical Institute⁵, UT Southwestern Medical Center, Dallas, TX 75390 USA; Department of Fundamental Neurosciences⁶, University of Lausanne, Lausanne, Switzerland; Center for Systems Biology⁷, Center for Computational and Integrative Biology⁸, and Gastrointestinal Unit⁹, Massachusetts General Hospital, Harvard Medical School, Boston, MA 02114 USA; Broad Institute of Harvard and MIT¹⁰, Cambridge, MA 02142 USA; Department of Immunology⁷, St. Jude's Children's Research Hospital, Memphis, TN 38105 USA

#Correspondence should be addressed: beth.levine@utsouthwestern.edu or JulienPierre.Puyal@unil.ch

*Present address: Department of Molecular Immunology and Inflammation, National Center for Global Health and Medicine, Tokyo, 162-8655, Japan

SUMMARY

A long-standing controversy is whether autophagy is a bona fide cause of mammalian cell death. We utilized a cell penetrating autophagy-inducing peptide, Tat-Beclin 1, derived from the autophagy protein Beclin 1, to investigate whether high levels of autophagy result in cell death by autophagy. Here we show that Tat-Beclin 1 induces dose-dependent death that is blocked by pharmacological or genetic inhibition of autophagy, but not of apoptosis or necroptosis. This death, termed “autosis”, has unique morphological features, including increased autophagosomes/autolysosomes and nuclear convolution at early stages, and focal swelling of the perinuclear space at late stages. We also observed autotic death in cells during stress conditions, including in a subpopulation of nutrient-starved cells *in vitro* and in hippocampal neurons of neonatal rats subjected to cerebral hypoxia-ischemia *in vivo*. A chemical screen of ~5,000 known bioactive compounds revealed that cardiac glycosides, antagonists of Na⁺,K⁺-ATPase, inhibit autotic cell death *in vitro* and *in vivo*. Furthermore, genetic knockdown of the Na⁺,K⁺-ATPase α 1 subunit blocks peptide and starvation-induced autosis *in vitro*. Thus, we have identified a novel form of autophagy-dependent cell death, an FDA-approved class of compounds that inhibit such death, and a crucial role for Na⁺,K⁺-ATPase in its regulation. These findings have implications for understanding how cells die during certain stress conditions and how such cell death might be prevented.

INTRODUCTION

The lysosomal degradation pathway of autophagy plays a crucial role in enabling eukaryotic cells to adapt to environmental stress, especially nutrient deprivation (1). The core autophagy machinery was discovered in a genetic screen in yeast for genes essential for survival during starvation, and gene knockout or knockdown studies in diverse model organisms provide strong evidence for a conserved pro-survival function of autophagy during starvation (1). This pro-survival function of autophagy results from its ability to mobilize intracellular energy resources to meet the demand for metabolic substrates when external nutrient supplies are limited.

In contrast to this well-accepted, pro-survival function of autophagy, there has been much debate as to whether autophagy – especially at high levels – also functions as a mode of cell death (2). Historically, based on morphological criteria, three types of programmed cell death have been defined, including Type I apoptotic cell death, Type II autophagic cell death, and Type III necrotic cell death (3). Autophagic cell death was originally defined as a type of cell death that occurs without chromatin condensation and is accompanied by large-scale autophagic vacuolization of the cytoplasm. This form of cell death, first described in the 1960's, has been observed ultrastructurally in tissues where developmental programs (e.g. insect metamorphosis) or homeostatic processes in adulthood (e.g. mammary involution following lactation or prostate involution following castration) require massive cell elimination (4-6). Autophagic cell death has also been described in diseased tissues and in cultured mammalian cells treated with chemotherapeutic agents or other toxic compounds (4-6).

The term “autophagic cell death” has been controversial, because it has been applied to scenarios where evidence is lacking for a causative role of autophagy in cell death (i.e. there is cell death “with autophagy” but not “by autophagy”). However, using more stringent criteria to define autophagic cell death (sometimes called “cell death by autophagy”), several studies in the past decade have shown that autophagy genes are

essential for cell death that occurs in certain tissues in invertebrate development (e.g. *Drosophila* midgut degradation and salivary gland destruction) as well as in cultured mammalian cells lacking intact apoptosis pathways – including *Bax*^{-/-}; *Bak*^{-/-} murine embryonic fibroblasts (MEFs) treated with DNA-damaging agents, mouse fibroblasts after caspase 8 inhibition, breast cancer cells with inactive caspase 3 that overexpress mutant Beclin 1, and myeloma cells after caspase 10 inhibition (6, 7). In apoptosis-competent cells, high levels of autophagy can also lead to autophagy gene-dependent, caspase-independent cell death, including in cells that express oncogenic H-Ras^{V12} (8) or a short isoform of p19^{ARF} (9), or that are exposed to various toxic agents (10). In neonatal mice, neuron-specific deletion of *Atg7* protects against cerebral hypoxia-ischemia-induced hippocampal neuron death (11), and in adult rats, shRNA targeting *beclin 1* decreases neuronal death in the thalamus that occurs secondary to cortical infarction (12).

While such studies provide genetic support for autophagy as a bona fide mode of cell death, the nature of autophagic cell death that occurs in mammalian cells and tissues in response to physiological/pathophysiological stimuli remains poorly defined. It is unclear whether cells that die “by autophagy” have unique morphological features or a unique death machinery. The only morphological feature that has been linked to autophagic cell death – autophagic vacuolization – may be observed in cells undergoing apoptotic or necrotic cell death, and no proteins aside from the core autophagy proteins have been shown to be required for autophagic cell death.

Here we identify a novel form of autophagic cell death, autosis, which has unique morphological features; depends on the cellular Na⁺,K⁺-ATPase; and occurs during treatment with autophagy-inducing peptides, starvation, and cerebral hypoxia-ischemia.

RESULTS

Autophagy-Inducing Peptides Trigger Autophagy-Dependent Cell Death. Previously, we discovered a potent autophagy-inducing cell permeable peptide (13), Tat-Beclin 1, composed of 11 amino acids of the HIV Tat protein transduction domain, a diglycine linker, and 18 amino acids (267-284) derived from the autophagy protein, Beclin 1. This peptide induced autophagy without cytotoxicity at low doses, but caused cell death at higher doses (13). This finding suggested that the Tat-Beclin 1 peptide might induce a form of autophagy-dependent cell death and serve as a model for defining characteristics of autophagy-dependent cell death that may occur in pathophysiological settings.

We examined the relationship between Tat-Beclin 1-induced autophagy and cell death. In HeLa cells, Tat-Beclin 1 led to dose-dependent induction of autophagy, as measured by ratios of LC3-II/I and degradation of the autophagy substrate, p62 (Fig. 1A) as well as cell death, as measured by a trypan blue exclusion assay (Fig. 1B). Increasing durations of exposure to a fixed concentration of Tat-Beclin 1 resulted in a time-dependent increase in autophagy and cell death (Fig. S1A-B). No autophagy induction or cell death was observed after treatment with a control peptide, Tat-Scrambled (13). Thus, Tat-Beclin 1 induces cell death in parallel with its ability to induce autophagy in a dose- and time-dependent manner.

We confirmed that Tat-Beclin 1 induced HeLa cell death by detection of cells positive for Sytox Green (a nucleic dye excluded by live cells) (Fig. 1C), an increase of propidium iodide (PI)-positive cells (Fig. S1C-D), and a decline of cellular ATP levels (Fig. S1E). In addition, Tat-Beclin 1, but not Tat-Scrambled (20 μ M, 5 h), significantly reduced clonogenic survival (Fig. 1D-E). Tat-Beclin 1 also induced cell death in a variety of additional tumor cell lines, in human and rat fibroblasts, and in both primary and E1A/Ras-transformed murine embryonic fibroblasts (MEFs) (Fig. S1F).

We investigated whether Tat-Beclin 1-induced autophagy is mechanistically related to Tat-Beclin 1-induced cell death by using pharmacological and genetic approaches to inhibit autophagy. Treatment with 3-methyladenine (3-MA), an inhibitor of Class III

phosphatidylinositol 3-kinase (PI3K) activity and autophagosome formation, partially blocked Tat-Beclin 1-induced HeLa cell death, as measured by a decreased percentage of trypan blue-positive cells (Fig. 1F), increased cellular levels of ATP (Fig. S1G), and increased clonogenic survival (Fig. 1G). siRNA knockdown of the essential autophagy gene, *beclin 1*, decreased autophagy in HeLa cells (as measured by p62 degradation) (Fig. S1H), and decreased Tat-Beclin 1-induced cell death, as measured by trypan blue exclusion (Fig. 1H) and clonogenic survival (Fig. 1I). Furthermore, doxycycline-inducible shRNA knockdown of *ATG13* or *ATG14* in U2OS cells decreased Tat-Beclin 1-induced autophagy (Fig. S1I) and protected against Tat-Beclin 1-induced cell death, as measured by trypan blue exclusion (Fig. 1J) and clonogenic survival (Fig. 1K). Blockade of autophagosomal/lysosomal fusion by bafilomycin A1, a vacuolar proton ATPase inhibitor, did not reduce Tat-Beclin 1-induced cell death (Fig. S1J), suggesting that this form of cell death does not require late stages of autophagy. In addition, another autophagy-inducing peptide, Tat-vFLIP $\alpha 2$ (which acts by releasing ATG3 from cellular FLIP) (14), also induced autophagy (Fig. S1K) that was associated with dose- and time-dependent cell death (Fig. S1L, S1M) which was reduced by *ATG14* knockdown in U2OS cells (Fig. S1N). Thus, autophagy-inducing peptides trigger cell death that requires the autophagy machinery.

Autophagy Peptide-Induced Death Does Not Require Apoptotic or Necroptotic Machinery. We next asked whether the apoptosis and/or necroptosis death machinery is involved in Tat-Beclin 1-induced cell death. We found that neither z-VAD, an inhibitor of caspases and apoptosis, nor necrostatin-1 (Nec-1), an inhibitor of RIPK1 kinase-mediated necroptosis, rescued Tat-Beclin 1-induced cell death as measured by trypan blue exclusion (Fig. 1F), levels of cellular ATP (Fig. S1G) or clonogenic survival (Fig. S2A). Adenovirus E1A/Ras-transformed MEFs with null mutations in the two pro-apoptotic genes, *Bax* and *Bak*, were susceptible to Tat-Beclin 1-induced cell death (Fig.

2A-B) but were resistant to death induced by the apoptosis-inducing agents, staurosporine and etoposide (Fig. S2B). Genetic deletion of two key regulators of necroptosis, *Ripk1* and *Ripk3*, failed to protect primary MEFs from Tat-Beclin 1-induced cell death (Fig. 2C-D). Thus, neither the apoptotic nor necroptotic death machinery is required for Tat-Beclin 1-induced cell death.

Additional assays confirmed the lack of apoptosis in Tat-Beclin 1-induced death. In contrast to staurosporine, Tat-Beclin 1 treatment did not activate caspase 3, as shown biochemically by the lack of cleavage of caspase 3 or its substrate PARP (Fig. 2E) and by the lack of immunofluorescence staining for active caspase 3 (Fig. 2F). In addition, minimal pan-caspase activity was detected in Tat-Beclin 1-treated cells, as measured by flow cytometry using a carboxyfluorescein-conjugated general caspase inhibitor, VAD-FMK (Fig. S2C-D). Consistent with non-apoptotic cell death, no TUNEL (terminal deoxynucleotidyl-transferase dUTP nick end labeling) staining (Fig. S2E) or DNA ladder formation (Fig. S2F) was detected in Tat-Beclin 1-treated cells. We also confirmed that Tat-Beclin 1 (derived from a structurally flexible region in the Beclin 1 evolutionarily conserved domain (15)) did not exhibit a pore-forming ability to release cytochrome *c* from mitochondria (Fig. S2G), as do certain other amphipathic α -helical peptides (16). Furthermore, various antioxidants that block ROS-mediated cell death failed to rescue Tat-Beclin 1-induced cell death (Fig. S2H). Similar to Tat-Beclin 1, Tat-vFLIP α 2 also failed to induce caspase 3 or PARP cleavage (Fig. S2I). Thus, taken together, our data indicate that autophagy-inducing peptide triggered cell death is genetically and biochemically distinct from apoptosis or necroptosis.

Autophagy Peptide-Induced Cell Death Has Unique Morphological Features. To characterize the nature of this autophagy-dependent, non-apoptotic and non-necrotic cell death, we performed live-cell imaging of Tat-Beclin 1-treated cells (Fig. 3A, Video S1, S2). During the initial phase after treatment, cells exhibit relatively normal morphology

with increased vacuolar dynamics and the perinuclear accumulation of numerous vacuoles. After a few hours, cells undergo an abrupt demise (lasting ~15-20 min) characterized by the rapid shrinkage of the nucleus with a portion of its surface developing a concave appearance corresponding to a round, vacuole-like entity, reflecting (based on our EM data; see below) a local separation of the inner and outer nuclear membranes. This is followed by focal plasma membrane rupture and extracellular extrusion of cytoplasmic contents. Cells treated with Tat-Beclin 1 display increased substrate adherence that persists until their final demise (unlike apoptotic or necrotic cells, which generally float).

The concave nuclear appearance observed in Tat-Beclin 1-induced cell death is associated with abnormalities in nuclear lamin A/C staining (lack of a uniform circular appearance and presence of focal regions of dense staining) (Fig. 3A, Fig. S3A). Tat-Beclin 1-treated dying cells also exhibit an abnormal fragmented pattern of Tom20 (mitochondrial marker) and PDI (endoplasmic reticulum [ER] marker) staining, and a striking increase in expression of LAMP1, a marker of late endosomes/autolysosomes (which would be expected in the setting of a robust autophagy response) (Fig. 3B). Tat-vFLIP $\alpha 2$ -treated dying cells have a similar concave nuclear appearance and similar abnormalities in lamin A/C, Tom 20, PDI, and LAMP1 staining (Fig. S3B).

We performed ultrastructural analyses to further characterize the morphology of Tat-Beclin 1-induced death (Fig. 3C, Fig. S3C). As apparent from live-cell imaging, there were two phases of the death process; phase 1 is characterized by a slow phase of gradual change and phase 2 is characterized by an abrupt phase of final collapse and cell death. Morphologically, phase 1 can be divided into two phases. In phase 1a, the nucleus becomes convoluted (but the perinuclear space is normal); chromatin is moderately condensed, forming darker regions in the nucleus with borders that are fuzzy (in contrast to clumps of chromatin that typically have sharp borders in apoptosis); many of the mitochondria are electron-dense and some have an abnormal internal structure (clumps

instead of bands); the ER is dilated and fragmented; and numerous autophagosomes, autolysosomes, and empty vacuoles are present. In phase 1b, the perinuclear space becomes swollen at discrete regions surrounding the inner nuclear membrane, and these swollen areas contain membrane-bound regions with a density and granularity resembling the cytosol. In some cases, the perinuclear space extends through substantial distances in the cytoplasm. In phase 2, there is focal ballooning of the perinuclear space (which appears empty), often associated with a concavity of the nuclear surface. At this late stage, the morphology appears necrotic; mitochondria and other organelles are swollen; and autophagosomes, autolysosomes, and ER are rare. There appears to be lysis of the plasma membrane (which is difficult to discern from EM analyses but is substantiated by the propidium iodide staining, Sytox Green staining, and live-cell imaging of Tat-Beclin 1-treated cells).

These ultrastructural changes are distinct from previously classifications of cell death (3), including type 3B “cytoplasmic death” (also called paraptosis) which also has perinuclear swelling. In type 3B cell death, the perinuclear swelling is moderate and uniform around the entire nuclear perimeter, whereas in death of autophagy-inducing peptide-treated cells, there is a pronounced ballooning in a focal region of the perinuclear space. To avoid confusion with terms such as “autophagic cell death” (which is sometimes applied to states in which it is not clear that autophagy is required for cell death and/or in which autophagic features co-exist with apoptosis or necrosis), we coined the term “autosis” to define cell death mediated by autophagy genes and characterized by focal perinuclear swelling. We note that several other studies have described “cell death by autophagy” i.e. cell death that is blocked by genetic inhibition of autophagy (6). However, to our knowledge, such studies have not described increased substrate adherence and focal perinuclear swelling of dying cells; thus, autosis represents a newly described form of cell death by autophagy.

Starvation Induces Autosis. We next investigated whether autosis occurs during physiological stress conditions associated with high levels of autophagy. Nutrient starvation is the most potent known physiological inducer of autophagy in eukaryotic cells, and previous studies have shown that autophagy delays apoptosis in cells subjected to starvation, including HeLa cells (1). However, upon subjecting HeLa cells to amino acid and serum starvation, we found that, unlike the vast majority of cells which detach from their substrate and undergo apoptosis (as evidenced by active caspase 3 staining), a small subpopulation (~1%) of cells become more substrate-adherent and lack evidence of caspase 3 activation (Fig. 4A). This population of substrate-adherent, caspase 3-negative cells undergoes plasma membrane rupture and cell death, as identified by Sytox Green staining (Fig. 4B), and also displays a marked increase (~3-fold) in number of autophagosomes (GFP-LC3 puncta) as compared to the number of autophagosomes in the majority population of starved cells that float and undergo apoptosis (Fig. 4C-D). These substrate-adherent cells have nuclei with concave regions and focal swelling of the perinuclear space (Fig. 4A-C, E) and display similar abnormalities in lamin A/C staining as observed in Tat-Beclin 1 and Tat-vFLIP $\alpha 2$ peptide-treated cells (Fig. 4B, Fig. S3B). Similar to Tat-Beclin 1 peptide treatment, we observed phase 1 starved cells with increased autophagosomes/autolysosomes, and regions of perinuclear swelling containing organelles as well as phase 2 cells with rare autophagosomes/autolysosomes and dilated regions in the perinuclear space (Fig. 4E). We also observed similar features of autosis in starved adherent bone marrow-derived murine macrophages (BMDMs) and primary MEFs (Fig. 4F), suggesting that starvation-induced autosis occurs in primary cells and is not merely a consequence of mutations that confer resistance to apoptosis in continuous cell lines. Moreover, the frequency of autotic cell death was higher (~5%) in primary cells compared to in HeLa cells.

To confirm that autophagy is required for starvation-induced death in cells with autotic morphology, we assessed the effects of autophagy gene knockdown on the

clonogenic survival of substrate-adherent starved cells. In this assay, floating (apoptotic and necrotic) cells were washed away after 48 h (HeLa cells) or 72 h (U2OS cells and BMDMs) starvation, and the clonogenic potential of the remaining adherent cells was assessed (Fig. S4A). Both *ATG7* and *beclin 1* siRNA treatment (Fig. S4B) increased numbers of colonies formed by starved adherent HeLa cells (Fig. 4G), and *ATG14* shRNA expression (Fig. S4C) increased numbers of colonies formed by starved adherent U2OS cells (Fig. 4H). Lysozyme:Cre-mediated deletion of *Atg5* (Fig. S4D) also increased numbers of colonies formed by starved adherent *Atg5*^{flox/flox} BMDMs (Fig. 4I). (*ATG7* siRNA, *beclin 1* siRNA, *ATG14* shRNA and *Atg5* deletion had minimal effect on the clonogenic survival of cells cultured in normal media (Fig. S4B-C, E)). Thus, autophagy genes are required for starvation-induced autosis.

Autosis Occurs during Rat Cerebral Hypoxic-Ischemic Injury. After establishing ultrastructural criteria for autosis in cultured cells, we evaluated whether autosis occurs *in vivo*. We performed electron microscopic analysis of neuronal death following cerebral hypoxia-ischemia in the brains of neonatal rats (Fig. 5); we focused on dying neurons in the hippocampus CA3 region because we had previously shown that most of these neurons degenerate with autophagic features (from 6 h after hypoxia-ischemia) without signs of apoptosis or necrosis (17). At 24 h after cerebral hypoxia-ischemia, most of the dying neurons displayed strong autophagic features such as numerous autophagosomes and autolysosomes, and empty vacuoles (phase 1a). Strikingly, some neurons also showed focal ballooning of the perinuclear space characteristic of phase 1b of autosis. Other dying neurons displayed the archetypal phase 2 feature of autosis, focal ballooning of the perinuclear space associated with nuclear concavity. Thus, autotic cell death occurs in certain pathophysiological settings *in vivo*.

A High-Throughput Chemical Screen Identifies Cardiac Glycosides as Potent Inhibitors of Autosis. To gain insight into the regulation of autosis, we performed high-throughput compound screening to identify inhibitors of Tat-Beclin 1-induced cell death, focusing on compound libraries consisting of bioactive agents with known targets. We measured levels of cellular ATP (as a proxy of cellular viability) 5 h after Tat-Beclin 1 treatment of HeLa cells in the presence of ~5,000 FDA-approved drugs and bioactive compounds with characterized mechanisms of action (Fig. S5A). We chose for further analysis the 36 top hits that had z-scores ≥ 3.0 in the primary screen (Fig. 6A, Table S1). These 36 hits were classified into 9 families based on their chemical structures and/or biological functions (Table S2). Of these 36 hits, 8 compounds demonstrated $> 40\%$ rescue of autosis in a repeat ATP assay and were chosen for further analysis (Table S3). Of these 8 compounds, only 5, including three cardiac glycosides (digoxin, digitoxigenin, and strophanthidin) and two purinergic receptor antagonists (suramin and NF 023) demonstrated more than 80% rescue of Tat-Beclin 1 peptide-induced cell death as measured by Sytox Green staining (Fig. S5B). The purinergic receptor antagonists, but not the cardiac glycosides blocked cellular peptide entry, as quantified by the cells that stained positive for a biotin-conjugated version of Tat-Beclin 1 in the presence of compound (Fig. S5C-D), and therefore, were not studied further. Thus, our chemical screen identified cardiac glycosides as the only class of agents that inhibited the Tat-Beclin 1-induced cell death without blocking cellular peptide entry.

To assess the significance of the effects of cardiac glycosides on autosis in an unbiased manner, we tested whether the nine cardiac glycosides present in our library were statistically enriched among top-scoring compounds. We calculated a weighted Kolmogorov-Smirnov-like statistic, the normalized enrichment score (NES), using Compound Set Enrichment Analysis (CSEA). CSEA demonstrated strong, highly significant enrichment for cardiac glycosides ($P < 10^{-4}$) (Fig. 6B). In addition to the three cardiac glycosides with z-scores ≥ 3.0 in the primary screen, we confirmed that other

cardiac glycosides in the compound libraries also exhibited a significant rescue effect (Table S4), as did a cardiac glycoside, neriifolin, which was not in the compound libraries and is known to exert neuroprotective actions (18) (Fig. S5E). We also performed CSEA using other previously identified compound sets for autophagy inducers, specific necrosis inducers, and specific apoptosis inducers (19); none of these sets were enriched among our top-scoring compounds (Fig. 6B). While there are previous reports that cardiac glycosides may induce basal autophagy (20, 21), an extensive set of autophagy inducers drawn from the literature were overrepresented among compounds that enhanced, rather than rescued, Tat-Beclin 1-induced cell death. The lack of concordance between compounds that inhibited autophagy, apoptosis, or necrosis with the rescue of Tat-Beclin 1-induced autosis is consistent with the latter representing a distinct death process.

Consistent with these bioinformatics analyses, the cardiac glycoside, digoxin, had no effect on apoptotic death induced by staurosporine or necrotic death induced by H₂O₂ (Fig. S5F-G) whereas digoxin, as well as digitoxigenin and strophanthidin, rescued Tat-Beclin 1-induced cell death with IC₅₀ values below 0.1 μM (Fig. S5H). Digoxin also rescued Tat-vFLIP α2-induced death in HeLa cells (Fig. S5H) and Tat-Beclin 1-induced cell death in U2OS cells (Fig. S5I). We also found that clonogenic survival was rescued in Tat-Beclin 1-treated HeLa cells by digoxin, digitoxigenin and strophanthidin (Fig. 6C); in Tat-vFLIP α2-treated HeLa cells by digoxin (Fig. 6D); and in the adherent subpopulation of HeLa cells subjected to prolonged starvation by digoxin (Fig. 6E) and neriifolin (Fig. 6F). Thus, cardiac glycosides rescue cell death triggered by multiple inducers of autosis.

Digoxin reversed the majority of morphological abnormalities in cells undergoing Tat-Beclin 1-induced autosis. By light microscopy, in the presence of digoxin, Tat-Beclin 1-treated cells displayed minimal nuclear abnormalities and lacked abnormal patterns of mitochondrial (Tom 20), ER (PDI), late endosome/lysosome (LAMP1), and nuclear

lamin A/C staining (Fig. 6G). At the ultrastructural level, the majority of digoxin-rescued cells demonstrated a normal shaped nuclear membrane without any focal swelling of the perinuclear space; intact ER structure; and the absence of increased numbers of autophagosomes and autolysosomes (Fig. 6H). The only morphological abnormality of autosis not reversed by digoxin in Tat-Beclin 1 treated cells was the presence of electron-dense mitochondria; however, digoxin alone (in the absence of Tat-Beclin 1) resulted in the appearance of electron-dense mitochondria (Fig. S5J). Together, these data indicate that digoxin reverses the morphological changes of autosis except for mitochondrial abnormalities, but these do not appear to be related to cell death.

We performed western blot analyses of LC3 and p62 and quantitation of GFP-LC3 puncta to further evaluate the effects of digoxin on autophagy. Under basal conditions, consistent with prior reports (20, 21), we observed a dose-dependent increase in LC3-II conversion and mild reduction in p62 levels (although we did not detect an increase in GFP-LC3 puncta) (Fig. 6I, Fig. S5K). In contrast, doses as low as 100 nM resulted in a mild decrease in starvation-induced autophagy and a more dramatic decrease in Tat-Beclin 1-induced autophagy, as measured by increased p62 protein levels, a mild decrease in the ratio of LC3-II/LC3-I, and a marked decrease in numbers of GFP-LC3 puncta (Fig. 6I, Fig. S5K). The increased p62 accumulation was not due to changes in *p62* mRNA expression (Fig. S5L). Although cardiac glycosides have been reported to induce apoptosis (22, 23), we did not observe caspase activation in Tat-Beclin 1-treated cells in the presence of digoxin (Fig. S5M).

The Na⁺,K⁺-ATPase Regulates Autosis. Cardiac glycosides are inhibitors of Na⁺,K⁺-ATPase, a plasma membrane pump that generates Na⁺ and K⁺ gradients across the membrane and acts as a versatile signal transducer (22). We therefore examined whether Na⁺,K⁺-ATPase regulates autosis using siRNA knockdown of the $\alpha 1$ subunit of *Na⁺,K⁺-ATPase*. Similar to digoxin treatment, *Na,K- $\alpha 1$* -subunit knockdown (Fig. S6A-B) resulted

in a mild decrease in starvation-induced autophagy and a more dramatic decrease in Tat-Beclin 1-induced autophagy (as measured by increased levels of p62 and decreased GFP-LC3 puncta) (Fig. 7A, Fig. S6A). The observed increase in p62 accumulation was not due to changes in *p62* mRNA expression (Fig. S6C) or to a block in peptide delivery into cells (Fig. S6D). In parallel with inhibition of autophagy, three different siRNAs against *Na,K-α1* inhibited Tat-Beclin 1- and Tat-vFLIP α2-induced death, as measured by a Sytox Green assay (Fig. 7B). They also increased clonogenic survival of Tat-Beclin 1-treated cells (Fig. 7C) and adherent cells subjected to starvation (Fig. 7D). *Na,K-α1* siRNA also exerted a protective effect against autosis in human U2OS (Fig. S6E-F) and in mouse NIH3T3 (Fig. S6G-H) cells. Digoxin did not enhance *Na,K-α1* siRNA-mediated protection against autosis triggered by autophagy-inducing peptides (Fig. S6I), suggesting that digoxin and Na⁺,K⁺-ATPase inhibition block autosis through the same mechanism.

Cardiac Glycoside-Mediated Protection Against Neuronal Autosis in Rat Cerebral Hypoxia-Ischemia. A previous chemical screen to identify compounds that provide neuroprotection in a mouse brain slice-based model for ischemic stroke revealed neriifolin as a strong hit, and whole animal studies have shown that neriifolin and other cardiac glycosides provide significant neuroprotection in neonatal models of cerebral hypoxia-ischemia (18, 24, 25). Given these observations, coupled with our findings described above that rat hippocampal CA3 region neurons die by autosis following hypoxia-ischemia, we evaluated whether neriifolin could protect neonatal rats against cerebral hypoxia-ischemia and reduce autosis in the hippocampal region CA3.

In agreement with a previous study in mice (18), we found that neriifolin was highly neuroprotective in rats; it dramatically increased the volume of intact tissue in the ipsilateral hemisphere of neonatal animals one week after cerebral hypoxia-ischemia (Fig. 8A-B). This effect was particularly notable in the hippocampus (Fig. 8B, Fig. S7A), where

significant neuronal pathology, especially in the CA3 region, was detected as early as 24 h after hypoxia-ischemia injury (Fig. S7B). The CA3 region of the hippocampus, as analyzed by examination of Nissl-stained sections, was protected at 24 h and 7 days after neonatal hypoxia-ischemia by neriifolin treatment as compared to vehicle-treated pups (Fig. S7A-B). In parallel with this neuroprotection, neriifolin prevented the increase in autophagy in the CA3 region of the hippocampus that occurred after hypoxia-ischemia injury, as measured by detection of decreased numbers of endogenous LC3 puncta and LAMP1 puncta by immunofluorescence and immunoperoxidase staining (Fig. 8C, S7C) and decreased levels of LC3-II (Fig. 8D-E). Strikingly, in contrast to the characteristic features of autosis (numerous autophagosomes, autolysosomes, and empty vacuoles; abnormal mitochondria and ER; focal separation of the inner and outer nuclear membrane) observed in the CA3 region of vehicle-treated pups 24 h after cerebral hypoxia-ischemia, the CA3 region neurons of neriifolin-treated animals displayed no ultrastructural features associated with autosis (Fig. 8F). Thus, cardiac glycosides block the increase in autophagy and protect hippocampal neurons against cerebral hypoxia-ischemia-induced autosis *in vivo*.

DISCUSSION

Our findings identify a novel form of autophagic cell death – autosis – that meets two essential criteria put forth by the cell death nomenclature committee (2); specifically (1) such death must be suppressed by inhibition of the autophagic pathway; and (2) such death must be distinct from apoptosis and necrosis. Although several studies have described cell death that meets these criteria, the role of autophagy as a mediator of cell death has remained controversial. The form of death that we observed in adherent cells subjected to starvation and in cells treated with autophagy-inducing peptides not only meets both these criteria for “autophagic cell death” but also has a distinctive morphological and chemical inhibition signature. In addition to the classical

morphological criteria of autophagic cell death (increased autolysosomes in dying cells lacking features of apoptosis and necrosis), death induced in starved adherent cells and by autophagy-inducing peptides is accompanied by ER dilation and stereotypic nuclear changes, involving an early convoluted appearance, the formation of focal concave regions of the nucleus with surrounding focal swelling of the perinuclear space, and the accumulation of structures within this space at early stages of the process. This form of cell death, but not apoptosis or necrosis, is also selectively blocked by pharmacological and genetic inhibition of Na^+, K^+ -ATPase.

Although the underlying mechanisms of the morphological changes of autosis and the pathway by which Na^+, K^+ -ATPase mediates autosis remain to be determined, the discovery of this unique morphological and chemical inhibition signature has important biological implications. Our findings pave the road to the discovery of physiological and pathophysiological conditions in which autophagy functions as a death mechanism, and may provide a candidate treatment for diseases in which such death contributes to pathogenesis. For example, using the morphological criteria we established for autosis in cells subjected to starvation or treatment with autophagy-inducing peptides, we identified the presence of autotic death in rat hippocampal neurons subjected to hypoxic-ischemic injury. Moreover, we showed that a class of FDA-approved chemical compounds – cardiac glycosides – that inhibited autosis in an *in vitro* chemical compound screen also reduced hippocampal neuronal autosis and conferred neuroprotection *in vivo* in neonatal rats subjected to cerebral hypoxia-ischemia. Thus, by defining a novel form of autophagic cell death and by performing an *in vitro* chemical screen that identified a specific class of inhibitors of this form of cell death (e.g. cardiac glycosides), we have been able to establish a scientific rationale for the use of cardiac glycosides in the treatment of a clinically important disease, neonatal cerebral hypoxia-ischemia. Based on our identification of specific morphological criteria for autosis, it should be possible to determine additional pathophysiological settings in which autosis plays a role and which

may be ameliorated by cardiac glycosides. Conversely, mediators in the regulatory network of autosis may serve as candidate targets in cancer chemotherapy or other settings where pharmacological induction of cell death may be beneficial.

We found that autosis occurs in at least two distinct physiological/pathophysiological conditions, starvation and cerebral hypoxia-ischemia. At present, it is not yet known which, if any, previously reported instances of autophagic cell death involve autosis (except for hypoxia-ischemia-induced hippocampal region CA3 death evaluated in this study). It is possible that the unique morphological changes we describe for autosis are present but have been missed in observations of autophagic cell death in other settings, especially those that lack concurrent features of apoptosis or necrosis and/or in tissues (e.g. heart and kidneys) where high levels of autophagy are postulated to play a role in ischemia-reperfusion injury (26, 27). While the future identification of specific biochemical markers of autosis will facilitate such investigations, it should be possible to determine whether cell death occurs via autosis using the morphological criteria we describe as well as studies examining the inhibitory effect of cardiac glycosides.

Although we are not aware of previous reports of similar nuclear morphological abnormalities in autophagic cell death, the expression of sterol reductases that are localized to the ER and outer nuclear membrane, TM7SF2 and DHCR1, results in massive ER and perinuclear space expansion resembling that observed in autotic cells (28). These observations suggest that disruption of ER/outer nuclear membrane cholesterol metabolism may produce the phenotype of ER and focal perinuclear space expansion. This phenotype is possibly caused by alterations of ER membrane properties including transport or channel conductance, which would result in osmotic changes and disruption of signaling through the nuclear envelope. Given the crucial role of the ER in autophagosomal biogenesis (29), we speculate that stimulation of very high levels of autophagy may perturb normal ER membrane biogenesis/homeostatic mechanisms, leading to similar expansions of the ER lumen and perinuclear space. Further studies are

needed to investigate the underlying mechanisms of the morphological abnormalities observed in autosis.

Cardiac glycosides, a large family of naturally-derived steroidal compounds, were first described for the treatment of heart diseases in 1785 (22). Approximately 50 years ago, Na^+, K^+ -ATPase was identified as the cellular target of cardiac glycosides. This membrane protein uses energy from hydrolysis of ATP to facilitate the transport of potassium ions into cells and sodium ions out of cells; inhibition of Na^+, K^+ -ATPase results in an increase in intracellular sodium and calcium ions. Cardiac glycosides also have diverse effects on cellular signaling, proliferation, metabolism, survival, gene expression, attachment, and protein trafficking. To our knowledge, cardiac glycosides have not previously been shown to inhibit autophagy or autophagic cell death, and in contrast, induce apoptosis in cancer cells (22). Our chemical screen revealed cardiac glycosides as the most potent inhibitors of autotic cell death, and we found that they inhibited both autophagy and autotic cell death in the setting of starvation, autophagy-inducing peptide treatment, and neonatal hippocampal hypoxic-ischemic injury.

The mechanism of action appears to be inhibition of the known target of cardiac glycosides, Na^+, K^+ -ATPase, as we observed similar effects with Na^+, K^+ -ATPase $\alpha 1$ subunit siRNA knockdown in human and mouse cells. We speculate that the known effects of the Na^+, K^+ -ATPase on increasing cell attachment (30) may contribute to the increased substrate adherence of cells undergoing autotic death. In addition, it is possible that nuclear envelope-associated Na^+, K^+ -ATPase activity (31) may alter membrane ionic transport and osmolarity and thereby, contribute to the ER and perinuclear space expansion observed in autotic cells.

Previous studies have shown that neriifolin and other cardiac glycosides reduce cerebral infarct size in rodent cerebral hypoxia-ischemia models (18, 24, 25); however, their mechanism of neuroprotection has been unknown. Our observations suggest that inhibition of autophagy and autophagy-dependent death pathways may be a central

mechanism of cardiac glycoside-mediated neuroprotection. Several cell death morphologies have been identified in different regions of the brain after neonatal hypoxic-ischemic injury, but neuron-specific deletion of *Atg7* or intracerebroventricular treatment with the autophagy inhibitor, 3-MA, is sufficient to reduce infarct lesion volume, indicating that autophagy may be upstream of multiple death pathways. This supports our previous recommendation that postischemic treatment of neonatal cerebral hypoxia-ischemia should target autophagy (17, 32). In the present study, we observed inhibition of autophagy and autotic cell death in hippocampal CA3 region neurons of rats treated with neriifolin, but the inhibition of autotic cell death in this region of the hippocampus is not sufficient to explain the dramatic reduction in overall ipsilateral infarct size following hypoxia-ischemia. Taken together with previous studies on autophagy, cell death and neonatal cerebral hypoxia-ischemia, the most likely explanation for the overall neuroprotection in neriifolin-treated rats is the blockade of both autophagy-dependent autotic death as well as other death pathways triggered by high levels of autophagy. Thus, cardiac glycosides and/or other agents targeting Na^+, K^+ -ATPase may not only ameliorate diseases associated with autotic cell death, but also diseases in which autophagy is upstream of other death execution pathways. We cannot definitely rule out indirect effects of neriifolin on neuroprotection, but these seem unlikely in view of our *in vitro* observations that cardiac glycosides inhibit stress-induced autophagy and autosis in a cell autonomous manner.

It is noteworthy that — during cerebral hypoxia or ischemia — the brain releases an endogenous form of cardiac glycoside (ouabain or endobain) that inhibits Na^+, K^+ -ATPase (33). Thus, by releasing its own inhibitor of Na^+, K^+ -ATPase in response to hypoxia-ischemia, the neonatal brain may have developed an important mechanism to reduce autophagy and cell death by autosis. A broader question is whether basal levels of endogenous cardiac glycosides may serve as a naturally occurring “brake” which

functions in multiple mammalian tissues to maintain autophagy at physiological levels that promote cell survival, rather than at pathological levels that promote cell death.

MATERIALS AND METHODS

Cell Culture. HeLa cells were obtained from ATCC (American Type Culture Collection). Information on the source of wild-type, *Ripk3*^{-/-}, *Ripk1*^{-/-};*Ripk3*^{-/-}, and *Bax*^{-/-};*Bak*^{-/-} MEFs, *Atg5*^{flox/flox} and *Atg5*^{flox/flox}-LysM-Cre BMDMs, and U2OS^{TetR}, U2OS^{TetR}/sh*ATG14*, and U2OS^{TetR}/sh*ATG13*, other cells used in this study, and culture conditions is provided in the SI Materials and Methods.

Autophagy-Inducing Peptides. Tat-Scrambled (YGRKKRRQRRRGVGNDFINHE TTGFATEW), Tat-Becn1 (YGRKKRRQRRRGGTNVFNATFEIWHDGEGFT), and Tat-vFLIP α2 (D-retro-inverso form, RRRQRRKKRGYGFVNLLFLVVE) (14) were synthesized and administered to cells as described (13).

Antibodies and siRNAs. See SI Materials and Methods for details of antibodies and siRNAs used in this study.

Cell Death Assays. See SI Materials and Methods for details of trypan blue staining, Sytox Green staining, CellTiter-Glo assays, propidium iodide staining, active caspase 3 detection, TUNEL staining, DNA fragmentation assays, and clonogenic survival assays.

Microscopy studies. Live cell imaging was performed using a Deltavision microscope in the UT Southwestern Live Cell Imaging Core. Immunofluorescent microscopic images were captured using a Zeiss Axioplan 2 microscope using staining protocols described in

the SI Materials and Methods. Immunofluorescence and immunohistochemical staining of rat brain sections was performed following hypoxia-ischemia as described in the SI Materials and Methods. Electron microscopy was performed on cells as described (13) and images were captured using a JEOL 1200 EX II Electron Microscope (UT Southwestern Electron Microscopy Core). Electron microscopy was performed on rat hippocampal sections as described (17) and sections were visualized using a Philips CM100 transmission electron microscope (Electron Microscopy Facility at the University of Lausanne). See SI Materials and Methods for information about Correlative Light Electron Microscopy (CLEM) experiments.

High-Throughput Chemical Screening. High-throughput chemical screening to identify inhibitors of Tat-Beclin 1-induced autosis was performed using CellTiter-Glo luminescent cell viability assays (Promega) with ~5,000 known bioactive compounds with characterized mechanisms, drawn from commercially available libraries: the Prestwick Chemical Library of FDA-approved drugs (Prestwick Chemical); LOPAC (Sigma-Aldrich); and the KBio3 library which includes the Spectrum (Microsource Discovery Systems), Biomol-NT (Biomol, now Enzo Life Sciences), and ICCB Known Bioactives (Enzo Life Sciences) collections. Details of the screening techniques and analyses are provided in the SI Materials and Methods.

Autophagy Analyses. Autophagy was assessed by fluorescent microscopic quantification of GFP-LC3 puncta in HeLa/GFP-LC3 cells as described (13), by immunostaining to detect LC3 and LAMP1 in rat brains, by western blot analysis of LC3 and p62 of cultured cells, and by electron microscopic analysis of cultured cells and rat brains.

Rat model of neonatal cerebral hypoxia-ischemia. Neonatal rat cerebral hypoxia-ischemia experiments were performed as described (17). Immediately after carotid artery occlusion, rat pups were injected intraperitoneally with either neriifolin (0.25 mg/kg diluted in 0.5% ethanol/PBS) (Sigma, S961825) or vehicle (0.5% ethanol/PBS). See SI Materials and Methods for details. All experiments were performed in accordance with the Swiss Laws for the protection of animals and were approved by the Vaud Cantonal Veterinary Office.

ACKNOWLEDGMENTS

We thank John Minna, Noboru Mizushima, Qiong Shi, Herbert Virgin, Xiaodong Wang, Qing Zhong, and Sandra Zinkel for providing critical reagents and protocols; Shuguang Wei for providing assistance with high-throughput screening; Beatriz Fontoura for helpful discussions; Zhongju Zou for technical support; Haley Harrington for assistance with manuscript preparation; the UT Southwestern Live Cell Imaging Facility; and the Electron Microscopy Facility of the University of Lausanne. This work was supported by NIH grants U54AI057156 and ROI CA109618 to B.L, RO1AI40646 to D.R.G., Contract HHSN268201000044C to S.Y.S., and by a Swiss National Science Foundation grant 310030-130769 to J.P., and by the NCI grants 1P01CA95471-09 (Dr. Steven McKnight) and 5P30 CA142543-03 (The Simmons Cancer Center) which support the UT Southwestern HTS Core Facility.

REFERENCES

1. Levine B, Kroemer G (2008) Autophagy in the pathogenesis of disease. *Cell* 132(1):27-42.
2. Galluzzi L, *et al.* (2012) Molecular definitions of cell death subroutines: recommendations of the Nomenclature Committee on Cell Death 2012. *Cell Death Differ* 19(1):107-120.
3. Clarke PG (1990) Developmental cell death: morphological diversity and multiple mechanisms. *Anat Embryol (Berl)* 181(3):195-213.

4. Lockshin RA, Zakeri Z (2004) Apoptosis, autophagy, and more. *Int J Biochem Cell Biol* 36(12):2405-2419.
5. Levine B, Yuan J (2005) Autophagy in cell death: an innocent convict? *J Clin Invest* 115(10):2679-2688.
6. Das G, Shrivage BV, Baehrecke EH (2012) Regulation and function of autophagy during cell survival and cell death. *Cold Spring Harb Perspect Biol* 4(6).
7. Lamy L, *et al.* (2013) Control of autophagic cell death by caspase-10 in multiple myeloma. *Cancer Cell* 23(4):435-449.
8. Elgendy M, Sheridan C, Brumatti G, Martin SJ (2011) Oncogenic Ras-induced expression of Noxa and Beclin-1 promotes autophagic cell death and limits clonogenic survival. *Mol Cell* 42(1):23-35.
9. Reef S, *et al.* (2006) A short mitochondrial form of p19ARF induces autophagy and caspase-independent cell death. *Mol Cell* 22(4):463-475.
10. Wu WK, *et al.* (2012) The autophagic paradox in cancer therapy. *Oncogene* 31(8):939-953.
11. Koike M, *et al.* (2008) Inhibition of autophagy prevents hippocampal pyramidal neuron death after hypoxic-ischemic injury. *Am J Pathol* 172(2):454-469.
12. Xing S, *et al.* (2012) Beclin 1 knockdown inhibits autophagic activation and prevents the secondary neurodegenerative damage in the ipsilateral thalamus following focal cerebral infarction. *Autophagy* 8(1):63-76.
13. Shoji-Kawata S, *et al.* (2013) Identification of a candidate therapeutic autophagy-inducing peptide. *Nature* 494(7436):201-206.
14. Lee JS, *et al.* (2009) FLIP-mediated autophagy regulation in cell death control. *Nat Cell Biol* 11(11):1355-1362.
15. Huang W, *et al.* (2012) Crystal structure and biochemical analyses reveal Beclin 1 as a novel membrane binding protein. *Cell Res* 22(3):473-489.
16. Pfeiffer DR, Gudz TI, Novgorodov SA, Erdahl WL (1995) The peptide mastoparan is a potent facilitator of the mitochondrial permeability transition. *J Biol Chem* 270(9):4923-4932.
17. Ginet V, Puyal J, Clarke PG, Truttmann AC (2009) Enhancement of autophagic flux after neonatal cerebral hypoxia-ischemia and its region-specific relationship to apoptotic mechanisms. *Am J Pathol* 175(5):1962-1974.
18. Wang JK, *et al.* (2006) Cardiac glycosides provide neuroprotection against ischemic stroke: discovery by a brain slice-based compound screening platform. *Proc Natl Acad Sci USA* 103(27):10461-10466.
19. Shen S, *et al.* (2011) Association and dissociation of autophagy, apoptosis and necrosis by systematic chemical study. *Oncogene* 30(45):4544-4556.
20. Hundeshagen P, Hamacher-Brady A, Eils R, Brady NR (2011) Concurrent detection of autolysosome formation and lysosomal degradation by flow cytometry in a high-content screen for inducers of autophagy. *BMC Biol* 9:38.
21. Wang Y, *et al.* (2012) Cardiac glycosides induce autophagy in human non-small cell lung cancer cells through regulation of dual signaling pathways. *Int J Biochem Cell Biol* 44(11):1813-1824.
22. Prassas I, Diamandis EP (2008) Novel therapeutic applications of cardiac glycosides. *Nat Rev Drug Discov* 7(11):926-935.

23. Newman RA, Yang P, Pawlus AD, Block KI (2008) Cardiac glycosides as novel cancer therapeutic agents. *Mol Interv* 8(1):36-49.
24. Kaur S, Rehni AK, Singh N, Jaggi AS (2009) Studies on cerebral protection of digoxin against ischemia/reperfusion injury in mice. *Yakugaku Zasshi* 129(4):435-443.
25. Dunn DE, *et al.* (2011) In vitro and in vivo neuroprotective activity of the cardiac glycoside oleandrin from Nerium oleander in brain slice-based stroke models. *J Neurochem* 119(4):805-814.
26. Suzuki C, *et al.* (2008) Participation of autophagy in renal ischemia/reperfusion injury. *Biochem Biophys Res Commun* 368(1):100-106.
27. Matsui Y, *et al.* (2007) Distinct roles of autophagy in the heart during ischemia and reperfusion: roles of AMP-activated protein kinase and Beclin 1 in mediating autophagy. *Circ Res* 100(6):914-922.
28. Zwerger M, Kolb T, Richter K, Karakesisoglou I, Herrmann H (2010) Induction of a massive endoplasmic reticulum and perinuclear space expansion by expression of lamin B receptor mutants and the related sterol reductases TM7SF2 and DHCR7. *Mol Biol Cell* 21(2):354-368.
29. Rubinsztein DC, Shpilka T, Elazar Z (2012) Mechanisms of autophagosome biogenesis. *Curr Biol* 22(1):R29-34.
30. Contreras RG, Shoshani L, Flores-Maldonado C, Lazaro A, Cerejido M (1999) Relationship between Na(+),K(+)-ATPase and cell attachment. *J Cell Sci* 112 (Pt 23):4223-4232.
31. Galva C, Artigas P, Gatto C (2012) Nuclear Na⁺/K⁺-ATPase plays an active role in nucleoplasmic Ca²⁺ homeostasis. *J Cell Sci* 125(Pt 24):6137-6147.
32. Puyal J, Ginet V, Clarke PG (2013) Multiple interacting cell death mechanisms in the mediation of excitotoxicity and ischemic brain damage: a challenge for neuroprotection. *Prog Neurobiol* 105:24-48.
33. De Angelis C, Hauptert GT, Jr. (1998) Hypoxia triggers release of an endogenous inhibitor of Na(+)-K(+)-ATPase from midbrain and adrenal. *Am J Physiol* 274(1 Pt 2):F182-188.

FIGURE LEGENDS

Fig 1. Tat-Beclin 1 induces autophagy-dependent cell death. (A) Western blot of LC3 and p62 in HeLa cells treated with Tat-Scrambled (T-S) or Tat-Beclin 1 (T-B) peptides for 5 h. (B) Cell death of HeLa cells treated T-S or T-B for 5 h. (C) Representative images of Sytox Green staining of HeLa cells treated with T-S or T-B (20 μ M, 5 h). Scale bar, 50 μ m. (D-E) Representative images (D) and quantification (E) of clonogenic cell

survival of HeLa cells treated with T-S or T-B (20 μ M, 5 h). (F) Death of HeLa cells treated with T-B (20 μ M, 5 h) + 10 mM 3-MA, 100 μ M z-VAD, or 100 μ M necrostatin-1 (Nec-1). (G) Clonogenic survival of HeLa cells treated with T-B (20 μ M, 4 h) \pm 10 mM 3-MA. (H) Cell death in siRNA-transfected HeLa cells treated with T-S or T-B (20 μ M, 5 h). (I) Clonogenic survival of siRNA-transfected HeLa cells treated with T-B (20 μ M, 3h). (J) Cell death of doxycycline (Dox)-inducible U2OS/TR, U2OS/shATG13 and U2OS/shATG14 cells \pm Dox (1 μ g/ml) for 5 days prior to treatment with T-S or T-B (20 μ M, 6 h). (K) Clonogenic survival of doxycycline (Dox)-inducible U2OS/TR, U2OS/shATG13 and U2OS/shATG14 cells \pm Dox (1 μ g/ml) for 5 days prior to treatment with T-B (25 μ M, 5 h). For B and E-K, bars represent mean \pm SEM and similar results were observed in three (B, F-K) or 5 (E) independent experiments. For E, G, I, and K, the number of colonies in untreated controls was standardized as 100%. NS, not significant; ** P <0.01; *** P <0.001; t-test. See also Fig. S1.

Fig. 2. Tat-Beclin 1-induced cell death does not require the apoptotic or necroptotic machinery. (A-B) Cell death (A) and clonogenic survival (B) of wild-type and *Bax*^{-/-}; *Bak*^{-/-} MEFs treated with peptide (5 h). (C-D) Cell death (C) and clonogenic survival (D) of wild-type, *Ripk1*^{+/+}; *Ripk3*^{-/-} and *Ripk1*^{-/-}; *Ripk3*^{-/-} MEFs treated with peptide (20 μ M, 5 h). In (B) and (D), the number of colonies of Tat-Scrambled-treated cells was standardized as 100%. (E) Western blot of cleaved caspase 3 and cleaved PARP in HeLa cells treated with 20 μ M Tat-Scrambled, 20 μ M Tat-Beclin 1, 1 μ M staurosporine \pm 100 μ M Z-VAD-FMK (z-VAD), or 32 mM H₂O₂ for 5 h. Asterisk denotes a cross-reacting band. (F) Representative images of cleaved caspase 3 staining in HeLa cells treated with 20 μ M Tat-Beclin 1 or 1 μ M staurosporine for 5 h. Scale bar, 50 μ m. For A-D, bars represent mean \pm SEM of triplicate samples and similar results were observed in three independent experiments. NS, not significant; *** P <0.001; t-test. See also Fig. S2.

Fig. 3. Morphological features of Tat-Beclin 1-induced autosis. (A) Representative live-cell imaging of HeLa cells treated with 25 μ M Tat-Beclin 1 for 5 h (Video S1, times shown as hh:mm). Black arrow denotes released intracellular components from a ruptured cell membrane and white arrow denotes a perinuclear space between the inner nuclear membrane and cytoplasm at a region of nuclear concavity. Scale bar, 10 μ m. (B) Representative images of mitochondrial (Tom20), ER (PDI), late endosome/lysosome (LAMP1), and nuclear lamin A/C staining in HeLa cells treated with Tat-Scrambled (T-S) or Tat-Beclin 1 (T-B) (20 μ M, 5 h). Scale bar, 20 μ m. (C) Electron microscopic analysis of HeLa cells treated with peptide (20 μ M, 5 h). White arrows show dilated and fragmented ER; black arrows show regions where the perinuclear space has swollen and contains clumps of cytoplasmic material. Scale bars, 1 μ m. See also Figure S3.

Fig. 4. Starvation induces autosis. (A) Representative images of active caspase 3 staining in HeLa cells 48 h after starvation (HBSS). Middle, active caspase 3-positive floating cells with rounded nuclei. Right, active caspase 3-negative adherent cell with concave nucleus and swollen perinuclear space. Scale bar, 20 μ m. (B) Representative image of a Sytox Green-positive adherent HeLa cell (top) and abnormal nuclear lamin A/C staining in an adherent HeLa cell (bottom) 48 h after starvation. Scale bars, 10 μ m. (C-D) Representative images (C) and quantitation (D) of GFP-LC3 dots (autophagosomes) in HeLa/GFP-LC3 cells (>50 cells analyzed per sample) grown in normal medium or in floating and adherent HeLa/GFP-LC3 cells 6 h after starvation. Scale bar, 10 μ m. (E) Upper row, electron microscopic images of a Phase 1 substrate-adherent HeLa cell 6 h after starvation. Lower row, correlative light-electron microscopy images of a Phase 2 substrate-adherent HeLa cell with concave nucleus and swollen perinuclear space (PNS) (arrow) 8h after starvation. Lower left, phase contrast microscopy; lower middle and lower right, electron microscopy of same cell. Black arrow in right lower panel shows outer nuclear membrane (ONM) and white arrow shows inner

nuclear membrane (INM). Scale bars, 1 μm . (F) Representative images of a Sytox Green-positive adherent primary murine BMDM and MEF 48 h after starvation. Scale bar, 10 μm . (G) Clonogenic survival of siRNA-transfected adherent HeLa cells starved for 48 h. NC, non-targeting control siRNA. (H) Clonogenic survival of doxycycline (Dox)-inducible adherent U2OS/TR and U2OS/sh*ATG14* cells \pm Dox treatment (1 $\mu\text{g}/\text{ml}$) for 5 days prior to starvation for 72 h. (I) Clonogenic survival of adherent BMDMs (two mice per genotype; *Atg5^{fl/fl}*; *Lyz-Cre-* and *Atg5^{fl/fl}*; *Lyz-Cre+* littermates) starved for 72 h. For D and G-I, bars represent mean \pm SEM of triplicate samples and similar results were observed in three independent experiments. For A-C and F, arrows denote concave nucleus and swollen perinuclear space. NS, not significant; ** $P < 0.01$; *** $P < 0.001$; t-test. See also Fig. S4.

Fig. 5. Morphological features of cerebral hypoxia-ischemia-induced autosis.

Electron microscopic analysis of dying neurons in hippocampal region CA3 in brains of 7-day-old rats 24 h after exposure to cerebral hypoxia-ischemia. Arrows show regions where the perinuclear space is swollen and contains clumps of cytoplasmic material. Scale bars, 1 μm . N, nucleus, PNS, perinuclear space; INM, inner nuclear membrane; ONM, outer nuclear membrane; ER, endoplasmic reticulum; GA, Golgi apparatus; M, mitochondrion.

Fig. 6. Cardiac glycosides rescue autosis. (A) Ranked distribution of z-scores for each compound in primary chemical screen (Table S1) for inhibitors of Tat-Beclin 1-induced cell death. Thirty-six top hits with $z \geq 3.0$ (Table S2) were selected for a secondary screen (Table S3). (B) Comparison of Compound Set Enrichment Analysis (CSEA) of cardiac glycosides in the primary autosis screening with compound sets of specific autophagy, necrosis, or apoptosis inducers. NES: normalized enrichment score. p = permutation P-value for the NES compared to a null distribution. Red-blue vertical bars

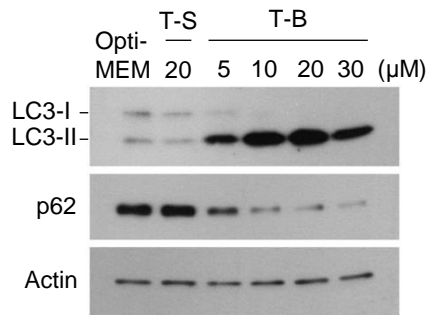
represent list of screened compounds, ranked according to z-score (greatest rescue of autosis at top). Each horizontal line indicates where a specific compound falls within ranked compound list. (C) Clonogenic survival of HeLa cells treated with Tat-Beclin 1 (20 μ M, 5 h) + 5 μ M digoxin, digitoxigenin or strophanthidin. The number of colonies of untreated cells was standardized as 100%. (D) Clonogenic survival of HeLa cells treated with 20 μ M Tat-Scrambled, 20 μ M Tat-Beclin 1, or 5 μ M Tat-vFLIP α 2 for 5 h \pm 5 μ M digoxin. The number of colonies of cells treated with Tat-Scrambled without digoxin was standardized as 100%. (E-F) Clonogenic survival of HeLa cells starved for 48 h \pm 10 nM digoxin (E) or 1 nM neriifolin (F). (Nanomolar concentrations were used as toxicity of digoxin and neriifolin was observed during starvation with micromolar concentrations.) (G) Representative images of mitochondrial (Tom20), ER (PDI), late endosome/lysosome (LAMP1), and nuclear lamin A/C staining in HeLa cells treated with 20 μ M Tat-Scrambled or Tat-Beclin 1 \pm 5 μ M digoxin for 5 h. Scale bar, 20 μ m. (H) Representative electron microscopic images of a HeLa cell treated with 20 μ M Tat-Beclin 1 + 5 μ M digoxin (5 h). Scale bar, 1 μ m. (I) Quantitation of GFP-LC3 dots (>100 cells analyzed per sample) in HeLa/GFP-LC3 cells treated with 20 μ M Tat-Beclin 1 or starved in HBSS for 2 h \pm 0.1 μ M digoxin and/or 20 nM bafilomycin A1. For C-F and I, bars represent mean \pm SEM of triplicate samples and similar results were observed in three independent experiments. NS, not significant; * P <0.05; ** P <0.01; *** P <0.001; t-test. See also Fig. S5, tables S1-S4.

Fig. 7. Na⁺,K⁺-ATPase regulates autosis. (A) Quantitation of GFP-LC3 dots (>100 cells analyzed per sample) in HeLa/GFP-LC3 cells 72 h after transfection with indicated siRNA and treatment with Tat-Beclin 1 (20 μ M, 2h) or starvation (HBSS, 2 h) \pm 20 nM bafilomycin A1. (B) Cell death measurement of HeLa cells transfected with indicated siRNA for 72 h, and then treated with Tat-Scrambled (20 μ M), Tat-Beclin 1 (20 μ M), or Tat-vFLIP α 2 (5 μ M) for 6 h. (C) Clonogenic survival of HeLa cells transfected with

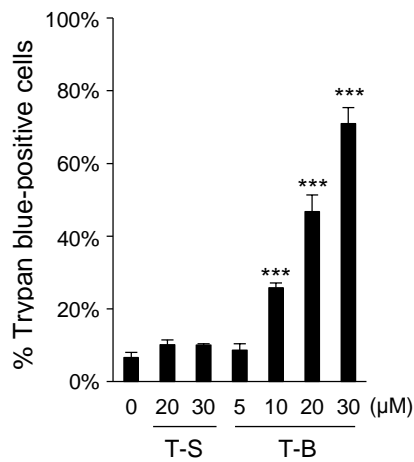
indicated siRNA for 72 h and then treated with Tat-Scrambled or Tat-Becn1 (20 μ M, 5 h). Shown are the percentage of colonies in Tat-Becn1- vs. Tat-Scrambled-treated cells for each siRNA. (D) Clonogenic survival of adherent HeLa cells transfected with indicated siRNA for 72 h, and then starved for 48h. Clonogenic survival of control siRNA transfected cells in starvation conditions relative to normal medium standardized as 100%. For A-D, bars represent mean \pm SEM of triplicate samples and similar results were observed in three independent experiments. NS, not significant; * P <0.05; ** P <0.01; *** P <0.001; t-test. See also Fig. S6.

Fig. 8. Neonatal hypoxic-ischemic brain damage and hippocampal CA3 region autophagy and autosis are reduced by treatment with the cardiac glycoside, neriifolin. (A) Representative Nissl-stained coronal sections through the brain showing the neuroprotective effect of neriifolin (bottom) as compared to vehicle (top) one week after HI. Scale bar, 1 mm. (B) Volumes of intact tissue ipsilaterally as compared to contralaterally one week after neonatal cerebral HI and indicated treatment. Values are mean \pm SD (n=6 for neriifolin and n=9 for vehicle). *** P <0.001; Welch's ANOVA test. (C) Representative confocal microscopy images of LC3 dots (red) and LAMP1 dots (green) in CA3 hippocampal neurons after 24h HI and indicated treatment or sham operation. NeuN (green) and MAP2 (red) are neuronal markers. Hoechst staining (blue) shows cell nuclei. Scale bars, 20 μ m. (D-E) Representative LC3 immunoblots (D) and quantification of LC3-II/tubulin levels (E) from immunoblots of hippocampi of rats subjected to HI. Values are mean \pm SD (n=6 for neriifolin and n=9 for vehicle). NS, not significant; * P <0.05; ** P <0.001; Kruskal-Wallis test. (F) Electron microscopic analysis of neriifolin effects in hippocampal region CA3 of 7-day-old rats 24 h after HI. PNS, perinuclear space; INM, inner nuclear membrane; ONM, outer nuclear membrane; N, nucleus; ER, endoplasmic reticulum; M, mitochondrion. Scale bars, 1 μ m.

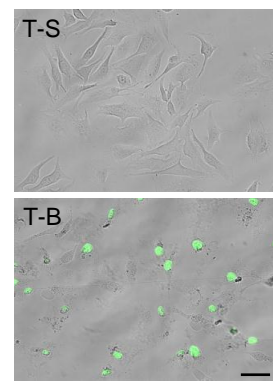
A



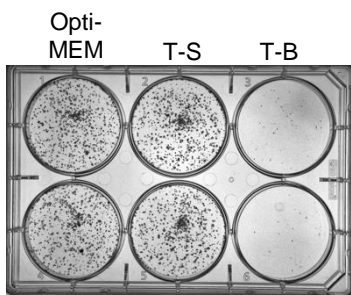
B



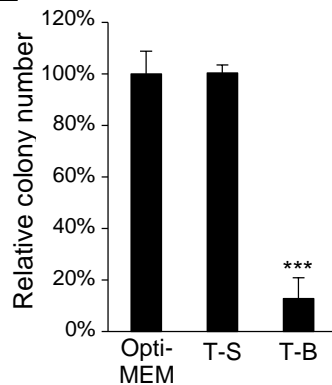
C



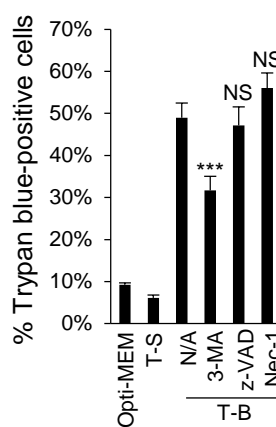
D



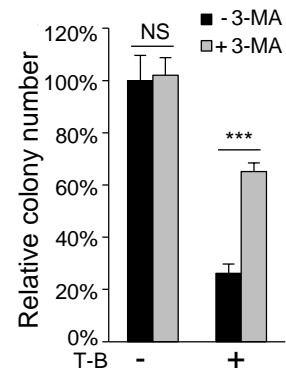
E



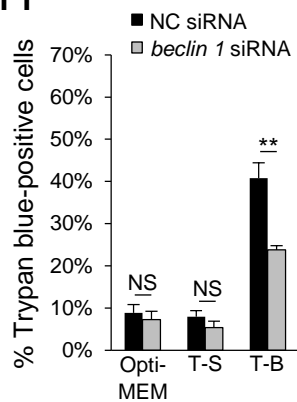
F



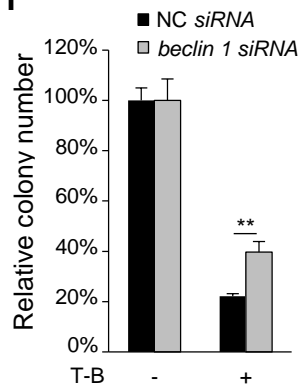
G



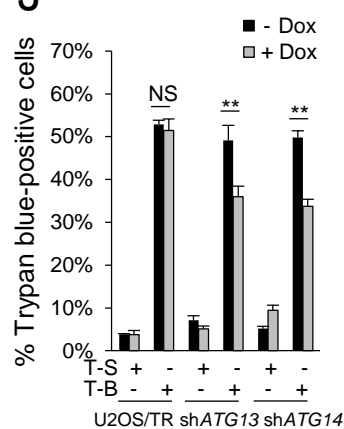
H



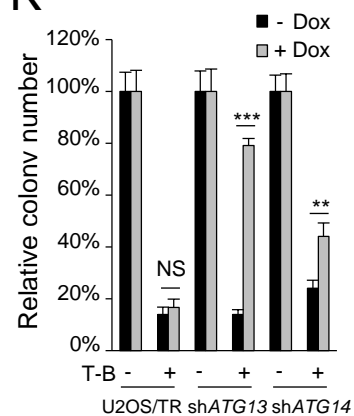
I

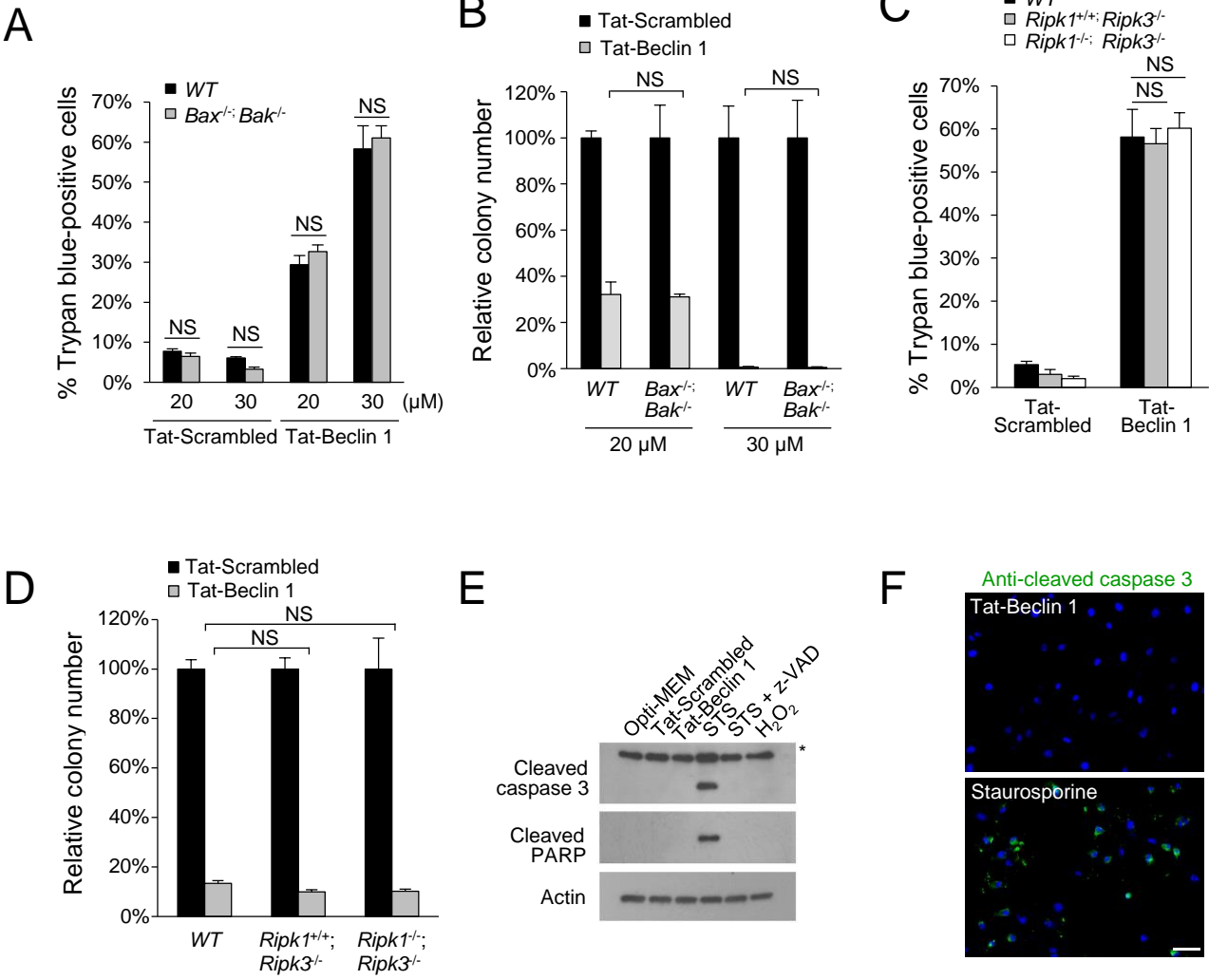


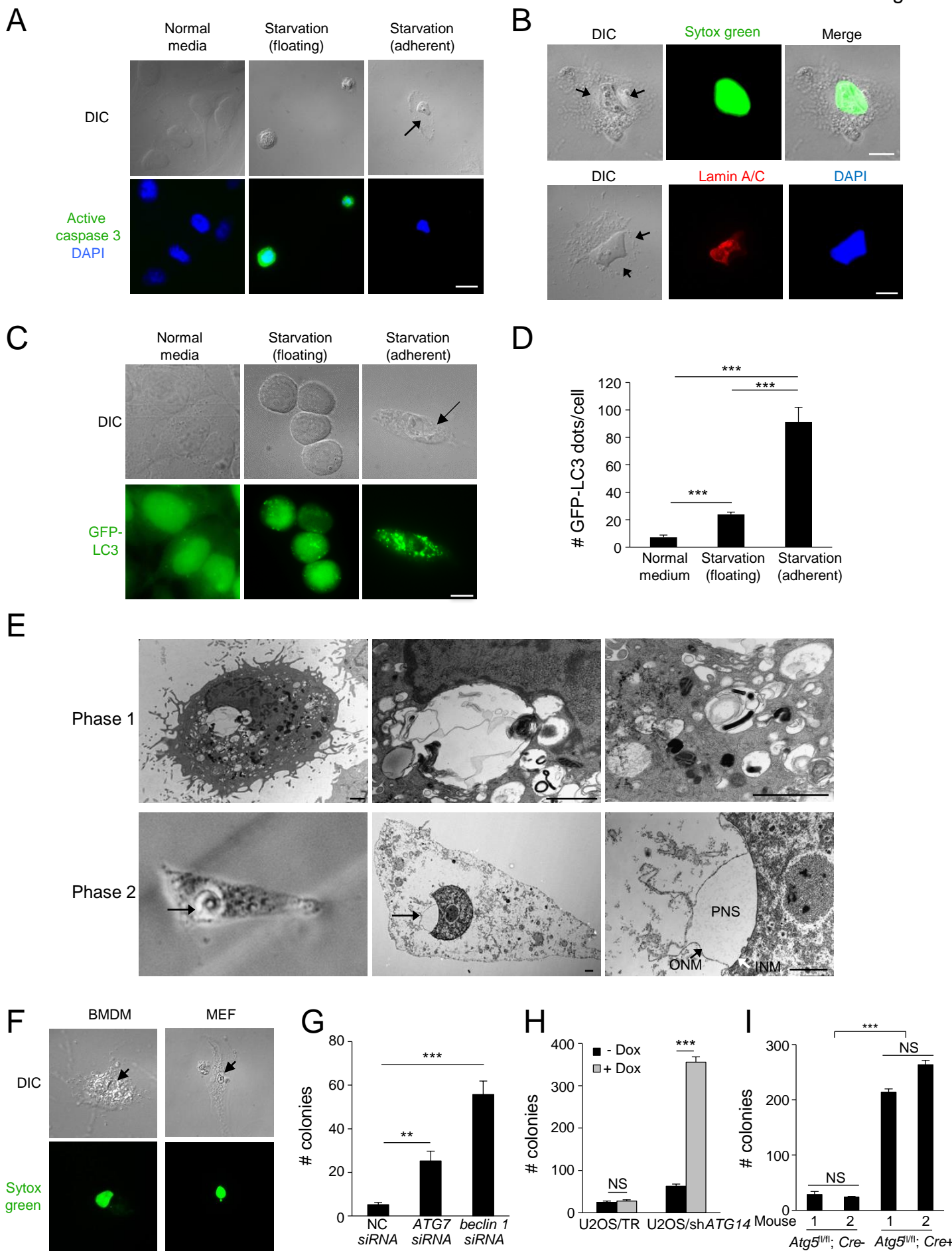
J

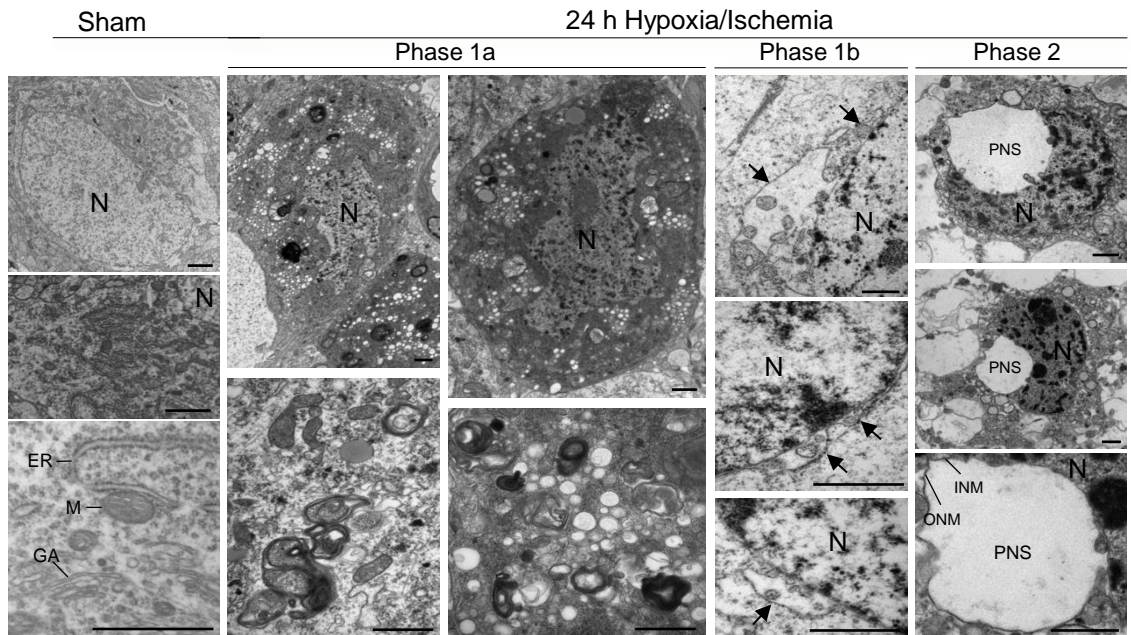


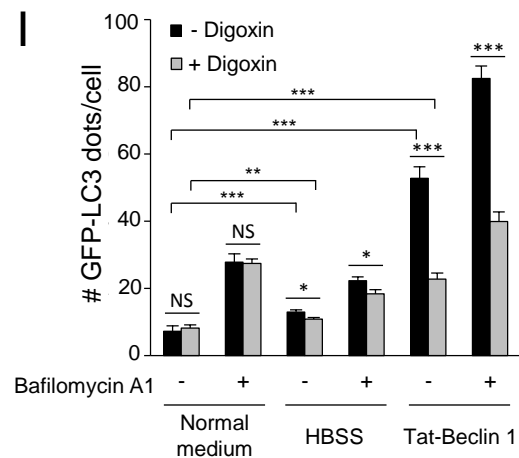
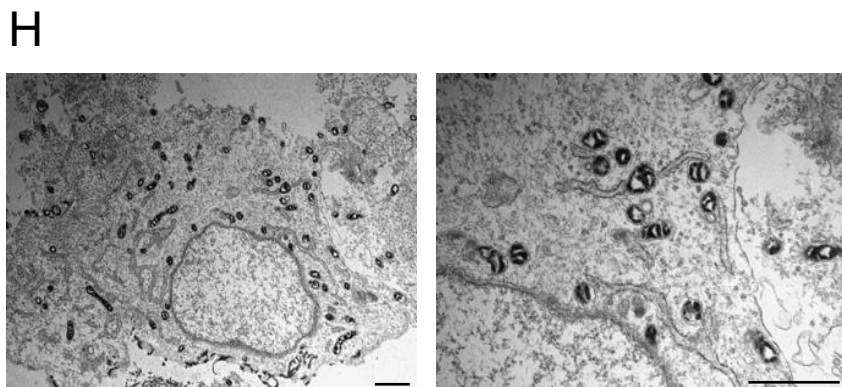
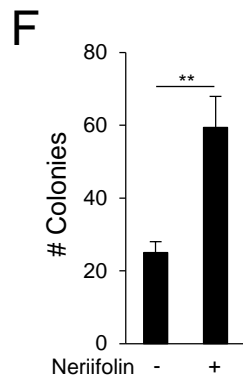
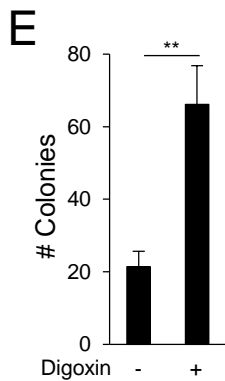
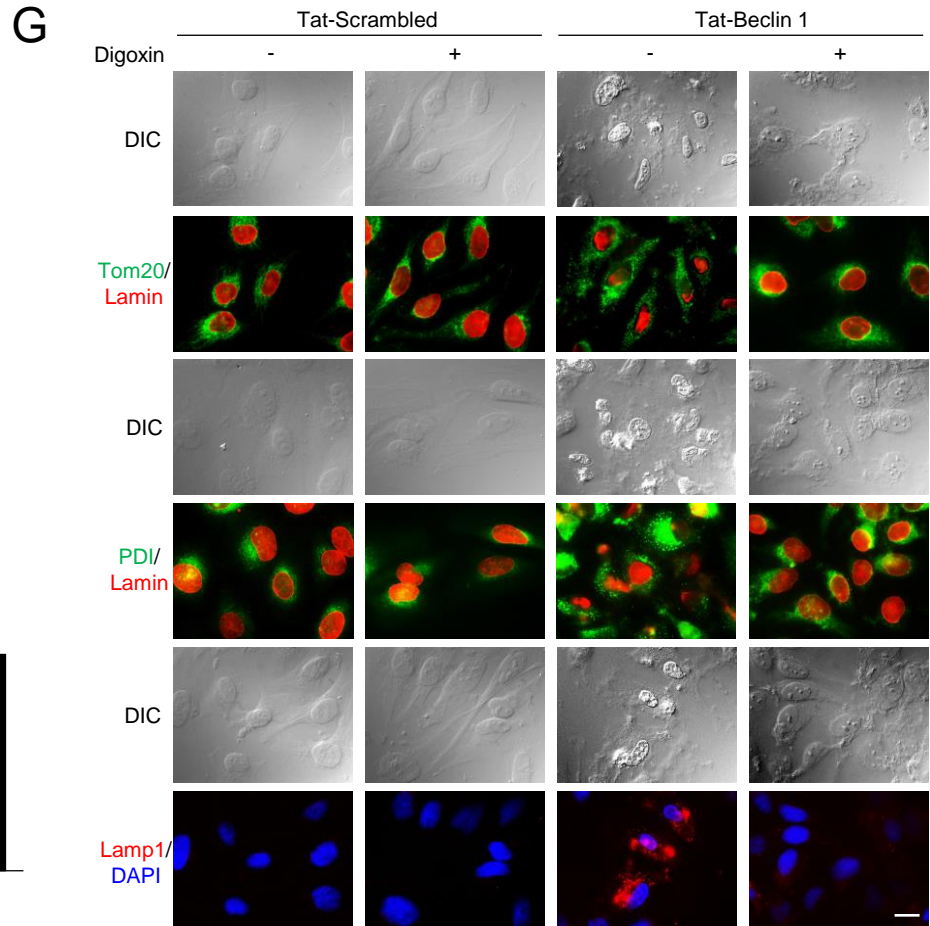
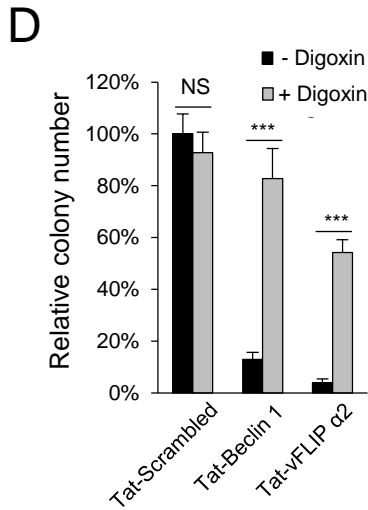
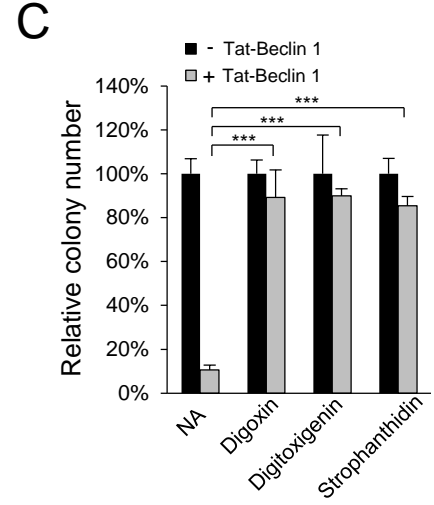
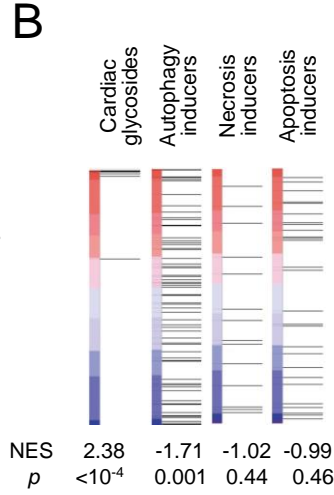
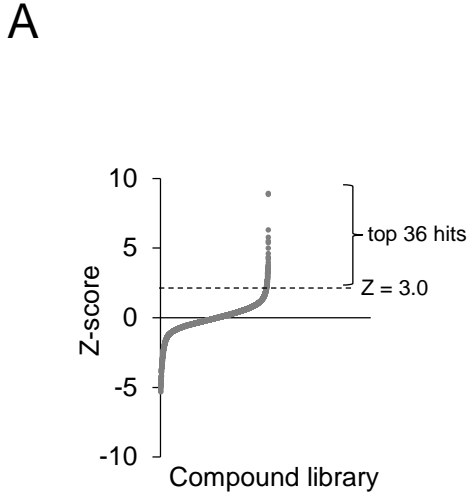
K



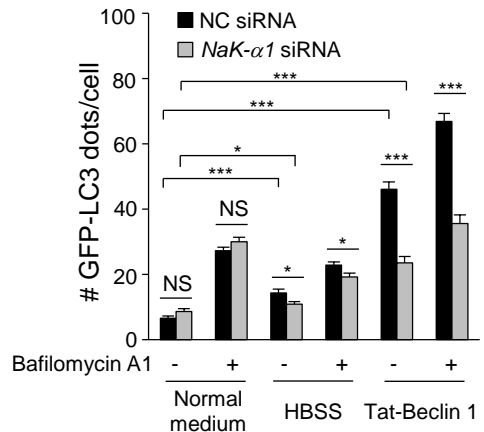




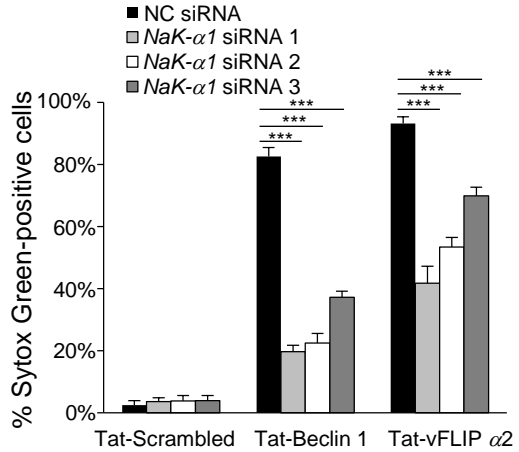




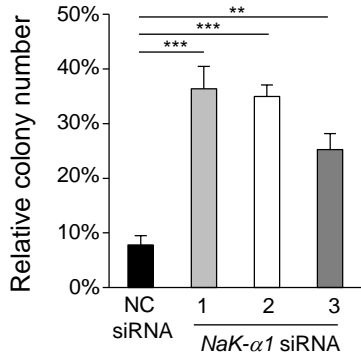
A



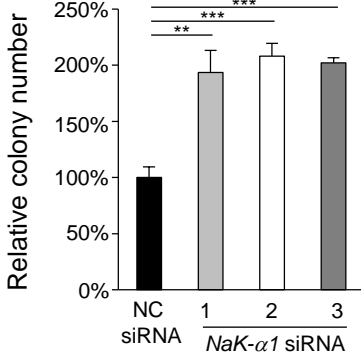
B



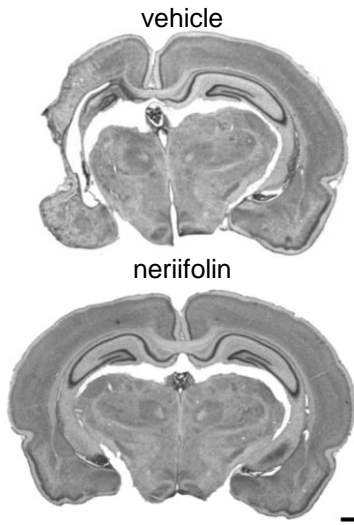
C



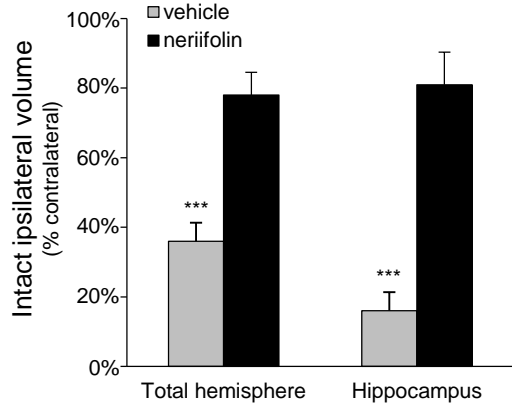
D



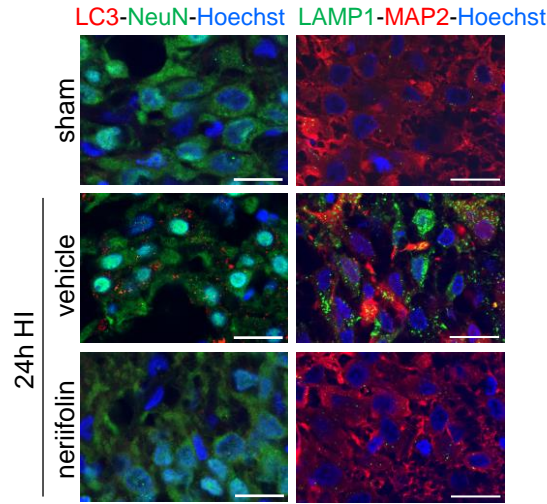
A



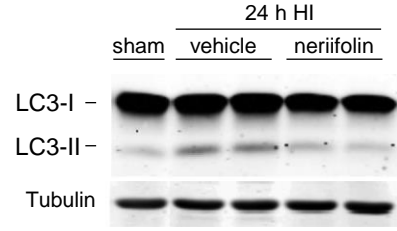
B



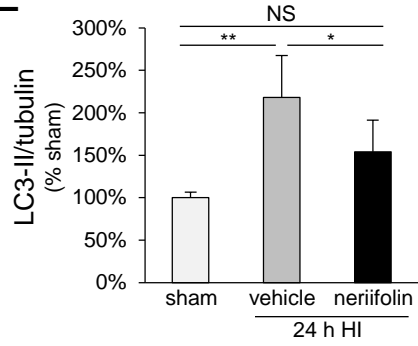
C



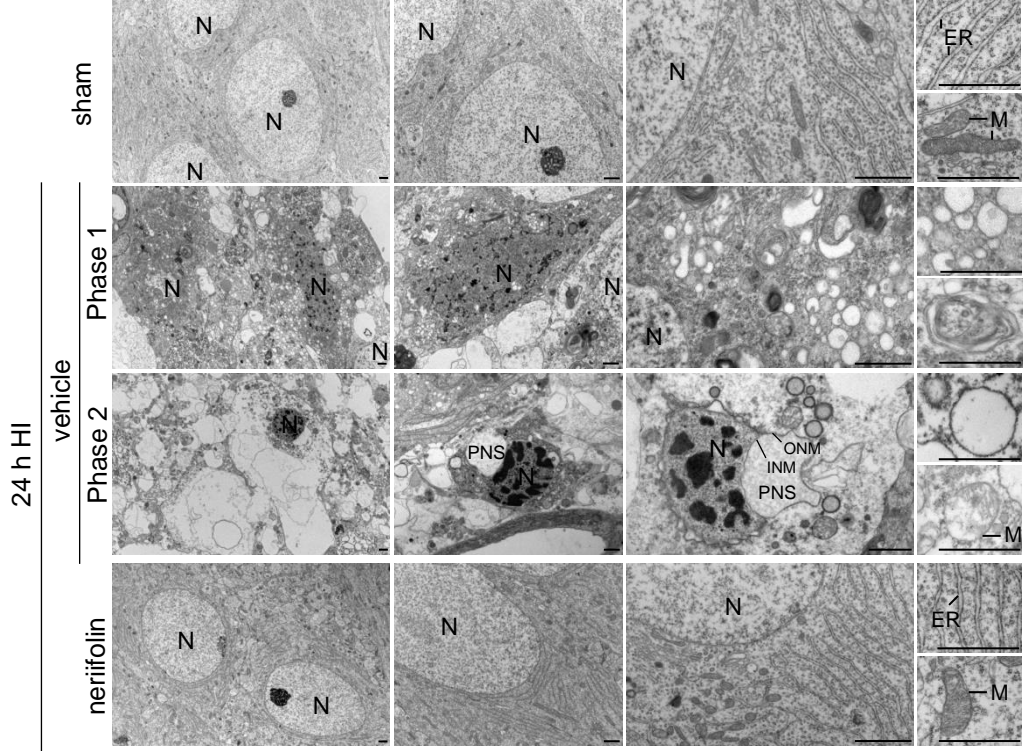
D



E



F



SUPPLEMENTARY INFORMATION

SI MATERIALS AND METHODS

Cell Culture. HeLa, MCF7, IMR90, Rat2 and NIH3T3 cells were obtained from ATCC (American Type Culture Collection). HCC827 and H1975 cells were obtained from Dr. John Minna (UT Southwestern Medical Center). U2OS cells were obtained from Dr. Sandra Zinkel (Vanderbilt University School of Medicine) (1). Primary wild-type, *Ripk3*^{-/-} and *Ripk1*^{-/-}; *Ripk3*^{-/-} MEFs were obtained as described (2, 3) from day e12 embryos. E1A-Ras transformed wild-type and *Bax*^{-/-}; *Bak*^{-/-} MEFs (4) were obtained as previously described (5). U2OS^{TetR} (U2OS/TR) and doxycycline-inducible U2OS cells expressing sh*ATG14/Barkor* (6) were obtained from Dr. Qing Zhong (University of California Berkeley). Doxycycline-inducible U2OS cells expressing sh*ATG13* (7) were obtained from Dr. Xiaodong Wang (National Institute of Biological Sciences, Beijing). Femurs from *Atg5*^{fl/fl}; *Lyz-Cre*⁻ and *Atg5*^{fl/fl}; *Lyz-Cre*⁺ littermate mice (8) were provided by Dr. Herbert Virgin (Washington University School of Medicine, St. Louis, Missouri) and bone marrow derived macrophages (BMDMs) were cultured as described.

HeLa, MCF7, U2OS and NIH3T3 cells were cultured in DMEM supplemented with 10% fetal bovine serum (FBS) and 1% penicillin/streptomycin. MEFs were cultured in DMEM supplemented with 20% FBS, 1×MEM non-essential amino acids, 1% penicillin/streptomycin and 0.1 mM β-mercaptoethanol. IMR90 and Rat2 cells were cultured in DMEM supplemented with 15% FBS, 1×MEM non-essential amino acids, 1% penicillin/streptomycin and 0.1 mM β-mercaptoethanol. HCC827 and H1975 cells were cultured in RPMI medium supplemented with 10% FBS and 1% penicillin/streptomycin. Doxycycline-inducible U2OS cells were cultured in Tet-approved FBS (Clontech, #631101) and then treated with 1 μg/ml doxycycline (Clontech, #631311) for 5 days. For

starvation experiments, cells were cultured in Hanks Balanced Salt Solution (HBSS) (Sigma, #H4641) for the indicated time period.

Chemical Reagents and Antibodies. The chemical reagents used in this study were: staurosporine (Fisher Scientific, #A380014C250), hydrogen peroxide (Sigma, #H1009), 3-methyladenine (Sigma, #M9281), z-VAD-FMK (Enzo Life Sciences, #ALX-260-020-M005), necrostatin-1 (Enzo Life Sciences, #BML-AP309), digoxin (Sigma, #D6003), digitoxigenin (Sigma, #D9404), strophanthidin (Sigma, #S6626), neriifolin (Sigma, #S961825), suramin (Sigma, #2671), NF 023 (Sigma, #N8652), niclosamide (Sigma, #N3510), quercetin (Sigma, #0020-05-95), myricetin (Sigma, #M6760), luteolin (Sigma, L9283), GP4G (Sigma, #D1262), nitrendipine (Sigma, #N144), miconazole (Sigma, #M3512), sulconazole (Sigma, #S9632), etoposide (Sigma, #E1383) and bafilomycin A1 (Sigma, #B1793).

The antibodies used for immunoblot analyses include: anti-LC3 (Novus Biologicals, #NB100-2220, 1:400 dilution for cell lysates; 1:1000 dilution for hippocampal lysates), anti-p62 (Abnova, #H00008878-M01, 1:2,000 dilution), anti-cleaved caspase-3 (Asp175) (Cell Signaling, #9661, 1:1,000 dilution), anti-cleaved PARP (Asp214) (Cell Signaling, #9541, 1:1,000 dilution), anti-Na⁺,K⁺-ATPase α 1 subunit (Santa Cruz Biotechnology, #sc-21712, 1:100 dilution), anti-Actin (Santa Cruz Biotechnology, #sc-47778, 1:20,000 dilution), anti-ATG13 (Sigma, #SAB4200100, 1:500 dilution), anti-ATG14 (MBL, #PD026, 1:200 dilution), anti-ATG5 (Novus Biologicals, #NB110-53818, 1:500 dilution), anti-Beclin 1 (Santa Cruz Biotechnology, #sc-11427, 1:500 dilution), anti-ATG7 (Sigma, #A2856, 1:500 dilution), anti-cytochrome *c* (Santa Cruz Biotechnology, #sc-13156, 1:1,000 dilution), and anti- α -tubulin (Santa Cruz Biotechnology, #sc-8035; 1:2000 dilution).

The antibodies used for immunofluorescence analyses of cultured cells include: anti-Tom20 (Santa Cruz Biotechnology, #sc-11415, 1:2,000 dilution), anti-PDI (Cell

Signaling, #3501, 1:200 dilution), anti-lamin A/C (Santa Cruz Biotechnology, #sc-6215, 1:200 dilution), and anti-LAMP1 (Santa Cruz Biotechnology, #sc-20011, 1:200 dilution). Active caspase 3 was detected by immunofluorescence using anti-cleaved caspase-3 (Asp175) (Cell Signaling, #9661, 1:400 dilution) antibody.

The antibodies used for immunohistochemical analyses of rat brain sections include: anti-microtubule associated protein 2 rabbit (Millipore, #AB5622; 1:200 dilution), anti-NeuN (Millipore, #MAB377; 1:200 dilution) and anti-LAMP1 (Calbiochem, #428017; 1:200 dilution). Anti-microtubule-associated protein 1 light chain 3 (LC3) was a gift from Professor Y. Uchiyama (Tokyo, Japan; 1:2,000 dilution).

Western Blot Analyses. For cultured cells, cell lysates were prepared by sonication in PBS buffer containing 1% NP-40, protease inhibitor cocktail (Roche Applied Sciences) and halt phosphatase inhibitor cocktail (Thermo Scientific). Protein concentrations of cell lysates were determined using the Bio-Rad Protein Assay (Bio-Rad, #500-0006). Proteins were separated by SDS-PAGE, transferred onto nitrocellulose membranes, and subjected to western blot analysis with the indicated antibodies.

For immunoblot analysis of tissue samples, the whole hippocampus was collected in lysis buffer (20 mM HEPES, pH 7.4, 10 mM NaCl, 3 mM MgCl₂, 2.5 mM EGTA, 0.1 mM dithiothreitol, 50 mM NaF, 1 mM Na₃VO₄, 1% Triton X-100 (reagents from Sigma-Aldrich), and a protease inhibitor cocktail (Roche)) 24 h after cerebral hypoxia-ischemia. Proteins were separated by SDS-PAGE, transferred onto nitrocellulose membranes and analyzed by immunoblotting. A blocking solution containing 0.1% casein and 0.1% Tween was used for dilution of primary antibodies. Protein bands were visualized using the Odyssey Infrared Imaging System (LI-COR). Odyssey v1.2 software (LI-COR) was used for densitometric analysis. Optical density values were normalized with respect to tubulin and expressed as a percentage of values obtained for sham-operated rat pups (100%).

siRNA Transfection. siRNAs targeting human *beclin 1* (GAGAGGAGCCAUUUAUUGA, CUAAGGAGCUGCCGUUAUA, GGAACUCACAGCUCCAUA and GAUACCG ACUUGUCCUUA) were purchased from Thermo Scientific on-target plus SMARTpool (L-010552-00-0005). siRNA targeting human *ATG7* (GGGUUAUUACUACAAUGGUGUU) was purchased from Dharmacon. Non-targeting siRNA was purchased from Thermo Scientific (D-001210-02-20). siRNAs targeting the human Na^+ , K^+ -ATPase α 1-subunit (No. 1: CUCGCUCACUGGUGAAUCA; No. 2: GAUUCGAAAUGGUGAGAAA; No. 3: CAUCCAAGCUGCUACAGAA) were purchased from Invitrogen (#4390824). siRNA targeting the α 1-subunit of mouse Na^+ , K^+ -ATPase (GGAUGAACUCCAUCGUAAA) was purchased from Invitrogen (#4390824). siRNA was transfected using Lipofectamine 2000 (Invitrogen) according to the manufacturer's instructions. After 72 h of transfection, cells were treated as described.

Immunofluorescence Staining of Cultured Cells. Cells were fixed using a 3% paraformaldehyde/2% sucrose solution and permeabilized with a Triton X-100 solution (0.5% Triton X-100, 20 mM HEPES pH7.4, 50 mM NaCl, 3 mM $MgCl_2$, 300 mM sucrose) or fixed using ice-cold methanol according to the manufacturer's instructions. The subcellular localization of organelle markers was detected by immunofluorescent staining and microscopy. For deconvolution analysis, cell images were captured using a Zeiss Axio Imager Z2 microscope and images were processed with AutoQuant X 2.2.2 and Imaris x64 7.5.0 software.

Correlative Light Electron Microscopy. For Correlative Light Electron Microscopy (CLEM), 1.6×10^5 cells were plated on a glass-bottom microwell dish (MatTek, #P35G-2-14-C-GRID) and cultured in HBSS for 8 h prior to fixation and EM analysis as

described in the main text. Brightfield images were captured using a Deltavision microscope in the UT Southwestern Live Cell Imaging Core.

Immunohistochemical and Immunofluorescence Analyses of Rat Brain Sections. For immunoperoxidase labelling of rat brain sections, quenching of endogenous peroxidases was first done in 0.3% H₂O₂ in methanol for 20 min and pre-incubation in 15% serum and 0.1% Triton X-100 in PBS for 45 min. Sections were then incubated overnight with the primary antibody in 1.5% serum and 0.1% Triton in PBS followed by 2 h with the biotinylated secondary antibody (Jackson ImmunoResearch) and detected using an avidin-biotin-peroxidase kit (VECTASTAIN Elite ABC Kit Vector, PK-6200) for 2 h at room temperature and incubation with diaminobenzidine (DAB, Roche, 11718096001) substrate solution. Sections were then dehydrated in graded alcohols and mounted in Eukitt mounting medium.

For immunofluorescence labeling, sections were first pre-incubated for 45 min in 15% serum and 0.1% Triton X-100 in PBS and then incubated overnight at 4°C with the primary antibody in 1.5% serum and 0.1% Triton in PBS, and then incubated for 2 h in fluorochrome-coupled secondary antibody (Alexa Fluor 488 or Alexa Fluor 594 from Molecular Probes) at room temperature. The sections were then rinsed in PBS and mounted with FluorSave (Calbiochem, #345-789-20) with or without Hoechst nuclear staining. An LSM 710 Meta confocal microscope (Carl Zeiss) was used for confocal laser microscopy. Confocal images were displayed as individual optical sections. For double-labeling, immunoreactive signals were sequentially visualized in the same section with two distinct filters, with acquisition performed in separated modes. Images were processed with LSM 710 software and mounted using Adobe Photoshop.

Cell Death Assays. The percentage of Trypan blue-positive cells was counted using Trypan blue (Bio-Rad #145-0021) for triplicate samples per condition with a minimum of

100 cells per sample. For Sytox Green staining, cells were cultured in Lab-Tek chamber slides (Thermo Scientific) and Sytox Green (100 nM) (Invitrogen, S7020) was added in the medium for one h following various treatments. After washing once with PBS, Sytox Green-positive cells were visualized using a Zeiss Axioplan 2 microscope, and counted for triplicate samples per condition with a minimum of 100 cells per sample. CellTiter-Glo assays were performed using CellTiter-Glo® Luminescent Cell Viability Kit according to the manufacturer's instructions (Promega, G7572). TUNEL staining was performed to detect apoptotic nuclei using the ApopTag Peroxidase *In Situ* Apoptosis Detection Kit according to the manufacturer's instructions (Millipore, #S7100). DNA ladder assays were performed using the genomic DNA purified from HeLa cells treated with 20 μ M Tat-Scrambled, 20 μ M Tat-Beclin 1 or 1 μ M staurosporine. Genomic DNA was purified by phenol/chloroform/isoamyl alcohol and precipitated by isopropyl alcohol. DNA concentration was measured by determining the OD₂₆₀ and 1 μ g DNA was loaded in each well. Annexin V-Propidium iodide staining, active caspase 3 detection, and clonogenic survival assays were performed as described below.

Flow Cytometry. For active caspase detection, HeLa cells were stained using the APO LOGIX Carboxyfluorescein Caspase Detection Kit (Cell Technology Inc, #FAM100-1). Briefly, cells were labeled with carboxyfluorescein (FAM)-VAD-FMK added to the culture medium for one additional h following various treatments. Cells were trypsinized and stained with propidium iodide according to the manufacturer's instructions. Cell population data were acquired using a FACS Calibur (UT Southwestern Flow Cytometry Core) and analyzed using Flowjo 8 software.

For Annexin V staining, HeLa cells were trypsinized and stained with AnnexinV-FITC (BioVision, #1101, 1:500 dilution) and 3.125 μ g/ml propidium iodide (Roche, #11348639001) in binding buffer (10 mM HEPES/NaOH, 150 mM NaCl, 5 mM KCl, 1 mM MgCl₂, 2 mM CaCl₂, pH 7.4) at room temperature for 15 min. Cell population data

were acquired using a FACS Calibur (UT Southwestern Flow Cytometry Core) and analyzed using Flowjo 8 software.

Clonogenic Survival Assays. Clonogenic survival assays were performed as described (9). Briefly, 1,000 cells/well were plated overnight in a 6-well plate. After treatment with Tat-Beclin 1 for the indicated time period, cells were allowed to recover in regular culture medium lacking any peptide for 4-10 days. To quantitate clonogenic survival, cells were washed once with PBS, fixed and stained with 6% glutaraldehyde and 0.5% crystal violet for 2 h. To evaluate clonogenic survival of adherent cells following starvation, cells were plated in a 6-well plate and cultured O/N to reach 80-90% confluency, and then cultured in HBSS for the indicated time period. After washing three times with PBS, cells were allowed to recover in normal medium for 7-10 days and similar methods were used to quantitate clonogenic survival.

***In vitro* Cytochrome *c* Release Assay.** Mouse mitochondria were isolated from the livers of wild-type C57/BL6 (8-10-week-old) mice as described (10). Fresh mitochondrial pellets were resuspended in buffer (10 mM HEPES, 250 mM sucrose, 1 mM ATP, 5 mM succinate, 0.08 mM ADP, 1 mM DTT, 2 mM K₂HPO₄, pH 7.4), and 50 µg was incubated with either Tat-Scrambled or Tat-Beclin 1 in 100 µl buffer at 37°C for 1 h. The supernatants and pellets were isolated by 10,000×g centrifugation at 4°C for 10 min. Eighty µl of each supernatant was boiled in 5× Laemmli buffer. The pellets were re-suspended with 80 µl buffer and boiled in 5× Laemmli buffer.

Peptide Entry Assay. N-terminal biotinylated Tat-Beclin 1 peptide (>95% purity as determined by RP-HPLC) was synthesized as described (11). For the peptide entry assay, cells were treated with 20 µM biotinylated Tat-Beclin 1 for 30 min, fixed with 4% paraformaldehyde at room temperature for 10 min, and permeabilized with Triton X-100

solution (0.5% Triton X-100, 20 mM HEPES pH7.4, 50 mM NaCl, 3 mM MgCl₂, 300 mM sucrose) for 5 min on ice. After staining with Alexa Fluor 488-conjugated streptavidin for 1 h, more than 400 cells were imaged using a Zeiss Axioplan 2 imaging microscope. Cells showing a typical intracellular staining pattern of Alexa Fluor 488 signal were counted as biotin-positive cells.

RT-PCR. Total RNA from 2×10⁵ HeLa cells was extracted and purified by an RNeasy Mini Kit (Qiagen) and 2 µg of RNA was subjected to reverse-transcription (Invitrogen) to obtain cDNA. Semi-quantitative RT-PCR was performed using the following primers: *actin* (5'-CATGTACGTTGCTATCCAGGC-3', 5'-CTCCTTAATGTCACGCACGAT-3'), *LC3B* (5'-CATGCCGTCGGAGAAGACCTTC-3', 5'-GTGTCCGTTACCAACAGGAAG-3'), and *p62* (5'-GACTACGACTTGTGTAGCGTC-3', 5'-AGTGTCCGTGTTTCACCTTCC-3').

Compound Screening and Data Analysis. For chemical compound screening, 1,500 HeLa cells/well were plated in 384-well plates (Corning, #3707) using a Multidrop instrument (MTX Lab System, Multidrop 384). The culture medium was aspirated and replaced with acidified Opti-MEM medium. Mock-treated (DMSO) cells and Tat-Beclin 1-treated cells with DMSO were included in each plate as standard controls. Compounds were added in triplicate using a Beckman FX liquid handler and incubated at 37°C/5% CO₂ for 30 min. Twenty µM Tat-Beclin 1 was then added to each well and incubated at 37°C/5% CO₂ for 5 h. The culture medium was aspirated off, and the measurement of cellular ATP levels was performed by adding 35 µl CellTiter-Glo solution (Promega, #G7573) per well and subsequent detection using an EnVision multimode plate reader. Compounds were assembled from commercially available libraries of FDA-approved drugs and known bioactive drugs with characterized mechanisms: Prestwick Chemical Library of FDA-approved drugs (Prestwick Chemical); LOPAC (Library of

Pharmacologically Active Compounds; Sigma-Aldrich); and the KBio3 library which includes the Spectrum Collection (Microsource Discovery Systems), Biomol-NT (Biomol, now Enzo Life Sciences), and ICCB Known Bioactives (Enzo Life Sciences).

Each compound was screened in triplicate. Using established data analysis pipelines (12, 13), replicate raw luminescence values were normalized, weighted for reproducibility across replicates, and converted to z-scores (where $z = (\text{weighted compound score} - \text{mean DMSO score}) / (\text{standard deviation of DMSO score})$). The Prestwick library was screened and analyzed independently at two different institutions (UT Southwestern, Massachusetts General Hospital) and the cardiac glycosides were strong hits in both screens, showing strong internal reproducibility.

For analysis of the Prestwick library compounds screened at the UT Southwestern high-throughput screening facility, experimental results obtained from EnVision multimode plate reader were analyzed using Genedata Screener[®] System (version 10). For each plate, the raw data values for all wells were normalized using Equation 1:

$$\text{Normalized Values} = \frac{\text{Raw Values} - \text{Median of Neutral Controls}}{\text{Median of Stimulatory Controls} - \text{Median of Neutral Controls}} \times 100$$

Then normalized values were corrected using Equation 2:

$$\text{Corrected Values} = \frac{\text{Normalized Values}}{\text{Correction Factor}}$$

, where the correction factor of a plate is calculated based on Genedata Screener[®] proprietary pattern detection algorithms. As each compound was assayed in triplicate in the screen, the three corrected values were condensed to a single value (condensed activity) using the "Robust Condensing" method in Genedata Screener[®], which is the most representative single value of the triplicates. In general, the triplicates were pre-condensed into a pair of values: $\text{Values}(X, Y) = (\text{Median of Triplicates } m) \pm \text{dispersion}$, where $\text{Dispersion} = \text{Median} (|X1-m|, |X2-m|, |X3-m|)$. The less X and Y differ ($|X - Y|$), the better the data quality. For data points with $|X - Y| \leq 30\%$ activity, the median of X and Y was used as the condensed activity, which is also the median of the triplicate

measurements. Otherwise, a condensing function $Max(X, Y)$ was used for determining the condensed activity.

Robust z-Score was then calculated for each compound using Equation 3:

$$\text{Robust Z-Score} = \frac{\text{Condensed Activity-Median of Neutral Controls}}{\text{Robust Standard Deviation of Neutral Controls}}$$

, where robust standard deviation is the standard deviation calculated using median of neutral controls instead of the mean of neutral control. Compounds tested later were ranked by Robust z-Score, and 36 compounds with Robust z-Scores higher than 3.0 were cherry picked and evaluated in confirmatory assays. Experimental results of the cherry-picked compounds were normalized using Equation 4:

$$\text{Normalized Values} = \frac{\text{Raw Values-Median of Neutral Controls}}{\text{Median of Neutral Controls}} \times 100$$

Then for each cherry-picked compound, the corrected value, condensed activity, and Robust z-Score were calculated using Equation 2 and Equation 3. More details of data analysis methods could be found in Genedata Screener[®] user documentation (14) or upon request.

For analysis of compounds from other libraries in screens performed at the Massachusetts General Hospital, replicate raw luminescence values for each compound were converted to a z-score using a standard analytic pipeline (12); in brief, $z = (\text{mean compound luminescence} - \text{mean DMSO luminescence}) / (\text{standard deviation of DMSO luminescence})$.

Compound Set Enrichment Analysis (CSEA) (12) utilized the GSEA module of the GenePattern software suite (broadinstitute.org/cancer/software/genepattern) (15) using standard settings for pre-ranked lists. CSEA is based on Gene Set Enrichment Analysis (16), which is widely used to identify sets of functionally related genes that are coordinately up- or down-regulated. CSEA calculates a permutation P-value for a given compound set using an established method, by randomly generating 1000 compound sets with the same number of compounds as the query set, and generating a null distribution from the normalized enrichment scores for these 1000 permuted compound sets. CSEA

analysis used ranked screening results from the Prestwick, Spectrum, Biomol and ICCB collections. In addition to cardiac glycosides, CSEA compound sets were drawn from the overlap between our screened compounds and those annotated by Shen *et al.* as specifically inducing apoptosis (Cluster-III), or necrosis (Cluster-IV) (17). In addition, the “Broad Autophagy Toolkit” is a collection of autophagy inducers that was compiled from the literature (18-25) and comprised the autophagy inducers in the CSEA compound set.

Neonatal Hypoxia-Ischemia Model. Hypoxia-ischemia (HI) was performed in 7-day-old male rats (Sprague Dawley of 16-19 g, from Janvier, France) according to the Rice-Vannucci modification of the Levine procedure (26). The rat pups were anesthetized with 3% isoflurane. The right common carotid artery was isolated, double-ligated and cut. Just after carotid occlusion, neriifolin (0.22 mg/kg diluted in 0.5% ethanol/PBS) (Sigma, S961825) or vehicle (0.5% ethanol/PBS) was injected intraperitoneally. After 2 h of recovery with the dam, pups were placed in a humidified chamber at 35.5°C with 8% oxygen. Two h of hypoxia was necessary to obtain a reproducible lesion volume. This HI protocol resulted in substantial damage affecting most of the ipsilateral hemisphere. After hypoxia, pups were returned to the dam until sacrifice. Sham animals underwent the surgical procedure but without ligation of the common carotid artery. For quantification of the intact tissue on the side ipsilateral to the lesion, rat pups were perfused with 4% paraformaldehyde in PBS (pH 7.4) one week after cerebral HI. Cryostat coronal serial sections (50 µm) were cut and stained with cresyl violet (Nissl staining). The areas of both intact brain hemispheres and of both hippocampi were measured in sections spaced at 500 µm using ImageJ software. The percentage of intact tissue was expressed as ipsilateral intact volume/contralateral volume × 100%.

Statistical Analyses. Statistical analysis of high-throughput compound screening was performed as described above. To compare the means of an experimental group with the control group in tissue culture studies, a student's t-test was used. For analysis of the data generated in the neonatal rat cerebral hypoxia-ischemia experiments, JB STAT software was used. Each group of data was first examined for distribution normality using Shapiro-Wilk tests. In cases of normal distribution, a Welch's ANOVA test (one-way ANOVA with unequal variances) was used followed by a post-hoc Tukey-Kramer test to compare the different treatments. When the distribution was not normal, a Kruskal-Wallis test (non-parametric analogue of the one-way ANOVA) was used followed by a post-hoc Steel-Dwass test to compare the different treatments.

REFERENCES

1. Liu Y, Bertram CC, Shi Q, Zinkel SS (2011) Proapoptotic Bid mediates the Atr-directed DNA damage response to replicative stress. *Cell Death Differ* 18(5):841-852.
2. Newton K, Sun X, Dixit VM (2004) Kinase RIP3 is dispensable for normal NF-kappa Bs, signaling by the B-cell and T-cell receptors, tumor necrosis factor receptor 1, and Toll-like receptors 2 and 4. *Mol Cell Biol* 24(4):1464-1469.
3. Kelliher MA, *et al.* (1998) The death domain kinase RIP mediates the TNF-induced NF-kappaB signal. *Immunity* 8(3):297-303.
4. Wei MC, *et al.* (2001) Proapoptotic BAX and BAK: a requisite gateway to mitochondrial dysfunction and death. *Science* 292(5517):727-730.
5. Zong WX, Lindsten T, Ross AJ, MacGregor GR, Thompson CB (2001) BH3-only proteins that bind pro-survival Bcl-2 family members fail to induce apoptosis in the absence of Bax and Bak. *Genes Dev* 15(12):1481-1486.
6. Sun Q, *et al.* (2008) Identification of Barkor as a mammalian autophagy-specific factor for Beclin 1 and class III phosphatidylinositol 3-kinase. *Proc Natl Acad Sci USA* 105(49):19211-19216.
7. Gao W, Shen Z, Shang L, Wang X (2011) Upregulation of human autophagy-initiation kinase ULK1 by tumor suppressor p53 contributes to DNA-damage-induced cell death. *Cell Death Differ* 18(10):1598-1607.
8. Zhao Z, *et al.* (2007) Coronavirus replication does not require the autophagy gene ATG5. *Autophagy* 3(6):581-585.
9. Franken NA, Rodermond HM, Stap J, Haveman J, van Bree C (2006) Clonogenic assay of cells in vitro. *Nat Protoc* 1(5):2315-2319.

10. Frezza C, Cipolat S, Scorrano L (2007) Measuring mitochondrial shape changes and their consequences on mitochondrial involvement during apoptosis. *Methods Mol Biol* 372:405-420.
11. Shoji-Kawata S, *et al.* (2013) Identification of a candidate therapeutic autophagy-inducing peptide. *Nature* 494(7436):201-206.
12. Shaw SY, *et al.* (2011) Disease allele-dependent small-molecule sensitivities in blood cells from monogenic diabetes. *Proc Natl Acad Sci USA* 108(2):492-497.
13. Seiler KP, *et al.* (2008) ChemBank: a small-molecule screening and cheminformatics resource database. *Nucleic Acids Res* 36(Database issue):D351-359.
14. Malo N, Hanley JA, Cerquozzi S, Pelletier J, Nadon R (2006) Statistical practice in high-throughput screening data analysis. *Nat Biotechnol* 24(2):167-175.
15. Reich M, *et al.* (2006) GenePattern 2.0. *Nat Genet* 38(5):500-501.
16. Subramanian A, *et al.* (2005) Gene set enrichment analysis: a knowledge-based approach for interpreting genome-wide expression profiles. *Proc Natl Acad Sci USA* 102(43):15545-15550.
17. Shen S, *et al.* (2011) Association and dissociation of autophagy, apoptosis and necrosis by systematic chemical study. *Oncogene* 30(45):4544-4556.
18. Williams A, *et al.* (2008) Novel targets for Huntington's disease in an mTOR-independent autophagy pathway. *Nat Chem Biol* 4(5):295-305.
19. Balgi AD, *et al.* (2009) Screen for chemical modulators of autophagy reveals novel therapeutic inhibitors of mTORC1 signaling. *PLoS One* 4(9):e7124.
20. Zhang L, *et al.* (2007) Small molecule regulators of autophagy identified by an image-based high-throughput screen. *Proc Natl Acad Sci USA* 104(48):19023-19028.
21. Hundeshagen P, Hamacher-Brady A, Eils R, Brady NR (2011) Concurrent detection of autolysosome formation and lysosomal degradation by flow cytometry in a high-content screen for inducers of autophagy. *BMC Biol* 9:38.
22. Pan J, *et al.* (2008) Autophagy induced by farnesyltransferase inhibitors in cancer cells. *Cancer Biol Ther* 7(10):1679-1684.
23. Yang PM, *et al.* (2010) Inhibition of autophagy enhances anticancer effects of atorvastatin in digestive malignancies. *Cancer Res* 70(19):7699-7709.
24. Bauer PO, *et al.* (2009) Inhibition of Rho kinases enhances the degradation of mutant huntingtin. *J Biol Chem* 284(19):13153-13164.
25. Aoki H, *et al.* (2007) Evidence that curcumin suppresses the growth of malignant gliomas in vitro and in vivo through induction of autophagy: role of Akt and extracellular signal-regulated kinase signaling pathways. *Mol Pharmacol* 72(1):29-39.
26. Rice JE, 3rd, Vannucci RC, Brierley JB (1981) The influence of immaturity on hypoxic-ischemic brain damage in the rat. *Ann Neurol* 9(2):131-141.

SUPPLEMENTAL FIGURE LEGENDS

Fig. S1. Autophagy-inducing peptides trigger cell death. (A) Western blot of LC3 and p62 in HeLa cells treated with 20 μ M Tat-Scrambled (T-S) or Tat-Becnin 1 (T-B) for indicated time points. (B) Cell death of HeLa cells treated with 20 μ M T-S or T-B for indicated time points. (C) Flow cytometry analysis of propidium-iodide (PI) and Annexin V staining in HeLa cells treated with T-B (20 μ M). Values represent percentage (mean \pm SEM) of PI⁺ and Annexin V⁺/PI cells for triplicate samples at each time point. (D) Flow cytometry analysis of propidium-iodide (PI) and Annexin V in HeLa cells 5 h after treatment with 20 μ M T-S, 20 μ M T-B, 1 μ M staurosporine, or 32 mM H₂O₂. Staurosporine was used as a control treatment for apoptosis induction and H₂O₂ was used as a control treatment for necrosis induction. Values represent percentage (mean \pm SEM) of Annexin V⁺/PI and PI⁺ cells for triplicate samples at each time point. (E) Cell viability (measured by CellTiter-Glo assay) of HeLa cells treated with 20 μ M T-S or T-B for indicated duration. The amount of ATP in untreated control cells (Opti-MEM) was standardized as 100%. (F) Sytox Green assay of indicated cell type treated with indicated peptide (20 μ M, 6 h). (G) Cell viability (measured by CellTiter-Glo assay) of HeLa cells treated with T-B (20 μ M, 5 h) in the presence of 10 mM 3-methyladenine (3-MA), 100 μ M z-VAD, or 100 μ M necrostatin-1 (Nec-1). The amount of ATP in untreated control cells (Opti-MEM) was standardized as 100%. (H) Western blot of Beclin 1 and p62 in HeLa cells transfected with indicated siRNA and then treated with T-B (20 μ M, 3 h). NC, non-targeting control siRNA. (I) Western blot of ATG13, ATG14, LC3 and p62 in doxycycline (Dox)-inducible U2OS/TR, U2OS/shATG13 and U2OS/shATG14 cells with or without Dox (1 μ g/ml) for 5 days prior to peptide treatment with T-B (20 μ M, 3 h). (J) Cell death (measured by Sytox Green assay) of HeLa cells treated with indicated concentration of Tat-Becnin 1 \pm 100 nM bafilomycin A1 (Baf A1) for 6 h. (K) Western blot of LC3 and p62 in HeLa cells treated with Tat-Scrambled (20 μ M), 20 Tat-Becnin 1

(20 μ M), or Tat-vFLIP α 2 (5 μ M) for 5 h. (L) Cell death (measured by Sytox Green assay) of HeLa cells treated with indicated concentration of Tat-vFLIP α 2 peptide for 5 h. (M) Cell death (measured by a Sytox Green assay) of HeLa cells treated with 5 μ M Tat-vFLIP α 2 peptide for indicated duration. (N) Cell death (measured by a Sytox Green assay) of doxycycline-inducible U2OS/TR and U2OS/sh*ATG14* cells treated with Tat-Scrambled or Tat-vFLIP α 2 peptides (5 μ M, 6 h). For B, E-G, J, and L-N, bars represent mean \pm SEM of triplicate samples and similar results were observed in three independent experiments. NS, not significant; * P <0.05; ** P <0.01; *** P <0.001; t-test.

Fig. S2. Tat-Beclin 1-induced cell death does not involve apoptosis or necroptosis and is not inhibited by antioxidants.

(A) Clonogenic survival of HeLa cells treated with Tat-Beclin 1 (20 μ M, 4 h) + 100 μ M z-VAD or 100 μ M necrostatin-1 (Nec-1). The number of colonies in untreated control cells was standardized as 100%. (B) Cell death (measured by trypan blue exclusion) of E1A/Ras-transformed wild-type and *Bax*^{-/-}; *Bak*^{-/-} MEFs treated with 1 μ M staurosporine or 20 μ M etoposide for 20 h. (C) Representative flow cytometry analysis of HeLa cells treated with 20 μ M Tat-Scrambled, 20 μ M Tat-Beclin 1, or 1 μ M staurosporine for 6 h or 32 mM H₂O₂ for 4 h and then stained for active caspase and propidium iodide (PI). (D) Quantification of the active caspase-positive population and active caspase-negative/PI-positive population shown in (C). (E) TUNEL assay of HeLa cells treated with 20 μ M Tat-Scrambled, 20 μ M Tat-Beclin 1, 1 μ M staurosporine or 32 mM H₂O₂ for 8 h. (F) DNA ladder assay of genomic DNA purified from HeLa cells treated with 20 μ M Tat-Scrambled, 20 μ M Tat-Beclin 1 or 1 μ M staurosporine for indicated time period. (G) Assessment of mitochondrial cytochrome *c* release in HeLa cells treated with Tat-Scrambled or Tat-Beclin 1 for 1 h. CaCl₂ (1 mM) and 0.5% Triton X-100 were used as positive controls. (H) Cell death (measured by a Sytox Green assay) of HeLa cells treated with 20 μ M Tat-Beclin 1 for 8 h + butylated hydroxyanisole (BHA, 100 μ M), propyl gallate (PG, 100 μ M), L-glutathione

reduced (GSH, 5 mM), or N-acetyl-L-cysteine (NAC, 10 mM). (I) Western blot of cleaved caspase 3 and cleaved PARP in HeLa cells treated with 20 μ M Tat-Scrambled, 20 μ M Tat-Becn1, 5 μ M Tat-vFLIP α 2, 1 μ M staurosporine \pm 100 μ M Z-VAD-FMK (z-VAD) for 5 h. For A-B, D, and H, bars represent mean \pm SEM of triplicate samples and similar results were observed in three independent experiments. NS, not significant; * P <0.05; *** P <0.001; t-test.

Fig. S3. Morphological features of Tat-Becn1-induced autosis. (A) Deconvoluted image of lamin A/C staining in HeLa cells treated with Tat-Becn1 (20 μ M, 5 h). Arrows denote concave areas of nuclei with surrounding perinuclear space in autotic cells. Scale bar, 20 μ m. (B) Representative images of Tom20, lamin A/C and PDI staining in HeLa cells treated with Tat-Scrambled (20 μ M), Tat-Becn1 (20 μ M) or Tat-vFLIP α 2 (5 μ M) peptides for 5 h and in substrate-adherent HeLa cells following 48 h starvation in HBSS. Black arrows indicate representative regions of nuclear concavity and/or enlarged perinuclear space. Scale bar, 20 μ m. (C) Electron microscopic analysis of HeLa cells treated with Tat-Scrambled or Tat-Becn1 (20 μ M, 5h). N, nucleus, PNS, perinuclear space; INM, inner nuclear membrane; ONM, outer nuclear membrane. White arrows show dilated and fragmented ER and black arrows show regions where the perinuclear space has swollen and contains clumps of cytoplasmic material. Scale bars, 1 μ m.

Fig. S4. Starvation induces autosis. (A) Schematic representation of clonogenic survival assay of adherent cells subjected to nutrient starvation. HBSS, Hanks Balanced Salt Solution. (B) Western blot of ATG7 and Becn1 in HeLa cells transfected with indicated siRNA for 72 h. Asterisks indicate cross-reacting bands. Quantification of clonogenic cell survival of siRNA transfected HeLa cells cultured in normal medium. The colony number of NC siRNA-transfected cells was normalized as 100%. (C) Western blot of ATG14 in doxycycline (Dox)-inducible U2OS/TR and U2OS/shATG14 cells \pm Dox

treatment (1 $\mu\text{g/ml}$ for 5 days). Quantification of clonogenic cell survival of U2OS/TR and U2OS/sh*ATG14* cells cultured in normal medium \pm 1 $\mu\text{g/ml}$ doxycycline. The colony number of cells without doxycycline was normalized as 100%. (D) Western blot of Atg5-Atg12 conjugate in primary bone marrow derived macrophages (BMDMs) from two *Atg5^{fl/fl}*; *Lyz-Cre-* and two *Atg5^{fl/fl}*; *Lyz-Cre+* littermate mice. (E) Quantification of clonogenic cell survival of BMDMs derived from two *Atg5^{fl/fl}*; *Lyz-Cre-* and two *Atg5^{fl/fl}*; *Lyz-Cre+* littermate mice cultured in normal medium. The colony number of *Atg5^{fl/fl}*; *Lyz-Cre-* BMDMs derived from the first mouse was normalized as 100%. For B, C, and E, bars represent mean \pm SEM of triplicate samples and similar results were observed in three independent experiments. NS, not significant; t-test.

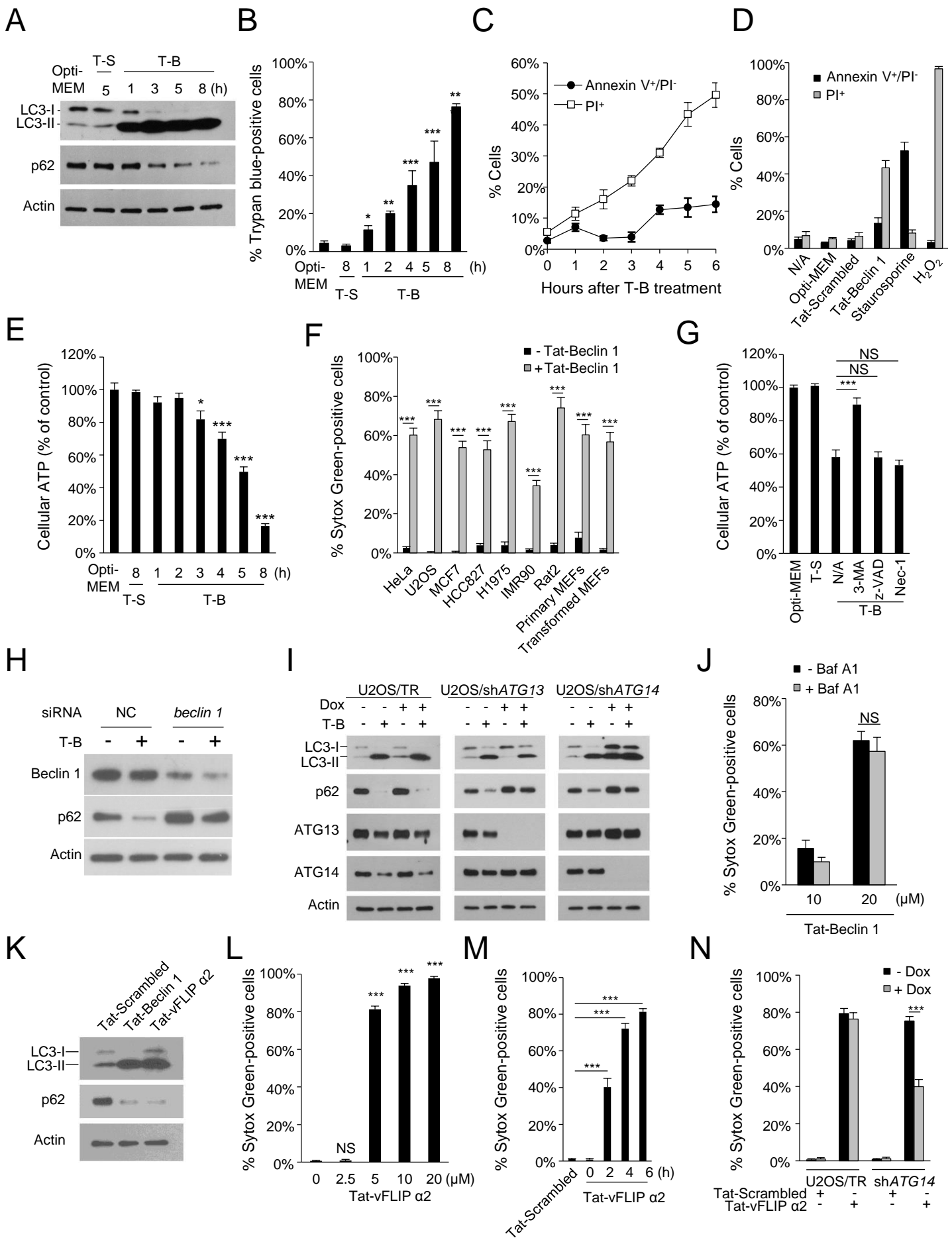
Fig. S5. Chemical screen to identify inhibitors of autosis. (A) Schematic diagram of high-throughput compound screening of inhibitors of Tat-Beclin 1-induced autosis in HeLa cells. See SI Materials and Methods for details. (B) Effects of compounds (10 μM) with greater than 40% rescue in Table S3 on percentage of cell death in Tat-Beclin 1-treated HeLa cells (20 μM , 5 h) as measured by Sytox Green-positive staining. Representative compounds with less than 40% rescue in Table S3 were also included as controls (luteolin, GP4G, nitrendipine, miconazole, sulconazole). (C) Immunofluorescence imaging of HeLa cells treated with Tat-Beclin 1 (T-B) or biotin-Tat-Beclin 1 (b-T-B) (20 μM , 30 min) + either digoxin (10 μM) or suramin (10 μM). Biotin-Tat-Beclin 1 was detected using Alexa Fluor 488 streptavidin. Scale bar, 50 μm . (D) Quantitation of percentage of cells containing intracellular biotin-Tat-Beclin 1 30 min following treatment with 20 μM peptide + either digoxin (10 μM) or suramin (10 μM). (E) Cell death (measured by Sytox Green staining) of HeLa cells after treatment with Tat-Beclin 1 (20 μM , 6 h) \pm 1 μM neriifolin. (F) Measurement of percentage of apoptotic cells (Annexin V⁺/PI) by FACS analysis in HeLa cells treated with 1 μM staurosporine \pm 5 μM digoxin for 5 h. (G) Cell death (measured by trypan blue exclusion)

of HeLa cells treated with 32 mM H₂O₂ ± 5 μM digoxin for indicated time period. (H) Cell death (measured by Sytox Green staining) of HeLa cells after treatment with Tat-Beclin 1 (20 μM, 6 h) or Tat-vFLIP α2 (5 μM, 6 h) in the presence of increasing concentrations of digoxin. Values are mean ± SEM of triplicate samples. Similar results were observed in three independent experiments. (I) Cell death (measured by Sytox Green staining) of U2OS cells after treatment with Tat-Beclin 1 (20 μM, 6 h) ± 5 μM digoxin. (J) Representative electron microscopic image of HeLa cells treated with 5 μM digoxin for 5 h. Scale bar, 1 μm. (K) Western blot of LC3 and p62 in HeLa cells following treatment with Tat-Beclin 1 (20 μM, 4h) (left gels) or after 4 h starvation (right gels) in the presence of indicated dose of digoxin. (L) Expression analysis of p62 and LC3B (measured by RT-PCR) in HeLa cells treated with Tat-Scrambled or Tat-Beclin 1 (20 μM, 4 h) or starved for 4 h ± 1 μM digoxin. (M) Western blot of cleaved caspase 3 and cleaved PARP in HeLa cells treated with Tat-Scrambled (20 μM), Tat-Beclin 1 (20 μM), or staurosporine (1 μM) ± 100 μM z-VAD or 5 μM digoxin for 5 h. For B, D-G, and I, bars represent mean ± SEM of triplicate samples and similar results were observed in three independent experiments. NS, not significant; *P<0.05;***P<0.001; t-test.

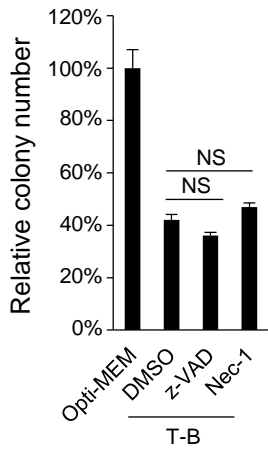
Fig. S6. Na⁺, K⁺-ATPase regulates autosis. (A) Western blot of LC3, p62 and the α1 subunit of Na⁺, K⁺-ATPase in siRNA transfected HeLa cells (72 h) treated with Tat-Beclin 1 (20 μM, 4 h) or starvation (4 h). (B) Western blot of Na⁺, K⁺-ATPase α1-subunit in HeLa cells transfected with a pool of three Na⁺,K⁺-ATPase α1 siRNAs (NaK-□/□ siRNA 1, NaK-□/□ siRNA 2, NaK-□/□ siRNA 3 shown in (A)) for 72 h. (C) Expression analysis of p62 and LC3 (measured by RT-PCR) in HeLa cells transfected with the indicated siRNA for 72 h and then treated with Tat-Scrambled or Tat-Beclin 1 (20 μM, 4 h) or starved for 4 h. (D) Quantitation of percentage of HeLa cells with intracellular biotin-Tat-Beclin 1 staining treated with 20 μM peptide for 30 min after NC-siRNA or

NaK- $\alpha 1$ siRNA transfection for 72 h. Biotin-Tat-Beclin 1 was detected using Alexa Fluor 488 streptavidin. (E) Western blot of Na⁺, K⁺-ATPase $\alpha 1$ -subunit in U2OS cells transfected with *Na⁺, K⁺-ATPase $\alpha 1$* siRNA 1 for 72 h. (F) Cell death (measured by Sytox Green staining) of U2OS transfected with indicated siRNA for 72 h and then treated with Tat-Scrambled or Tat-Beclin 1 (20 μ M, 6 h). (G) Western blot of Na⁺,K⁺-ATPase $\alpha 1$ -subunit in NIH3T3 cells transfected with *NaK-□* siRNA (mouse) for 72 h. (H) Cell death (measured by Sytox Green staining) of NIH3T3 cells transfected with indicated siRNA for 72 h and then treated with Tat-Scrambled or Tat-Beclin 1 (20 μ M, 6 h). (I) Cell death (measured by Sytox Green staining) of HeLa cells transfected with indicated siRNA for 72 h, and then treated with Tat-Scrambled (20 μ M), Tat-Beclin 1 (20 μ M), or Tat-vFLIP $\alpha 2$ (5 μ M) + 10 μ M digoxin for 6 h. For D, F, and H-I, bars represent mean \pm SEM of triplicate samples and similar results were observed in three independent experiments NS, not significant; *** $P < 0.001$; t-test.

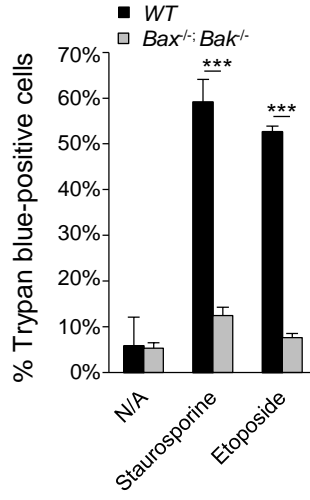
Fig. S7. Neonatal hypoxic-ischemic brain damage and hippocampal CA3 region autophagy and autosis are reduced by treatment with the cardiac glycoside, neriifolin. (A) Nissl-stained sections showing the effects of neriifolin treatment on the hippocampus one week after hypoxia-ischemia (HI). Neriifolin treatment protected almost all the hippocampus (lower panels) including the CA3 region (lower right panel) compared to vehicle-treated pups exposed to HI (middle panels). Scale bars, 100 μ m. (B) Nissl-stained sections showing the effects of neriifolin treatment on the CA3 region of the hippocampus 24 h after HI exposure in rat pups treated with vehicle or neriifolin. Scale bars, 100 μ m. (C) Immunohistochemistry to detect LC3 and LAMP1 in the CA3 region of the hippocampus 24 h after neonatal HI with indicated treatment. Scale bars, 100 μ m (low magnifications); 20 μ m (high magnifications).



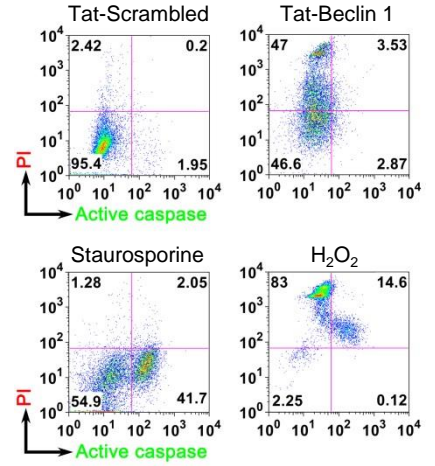
A



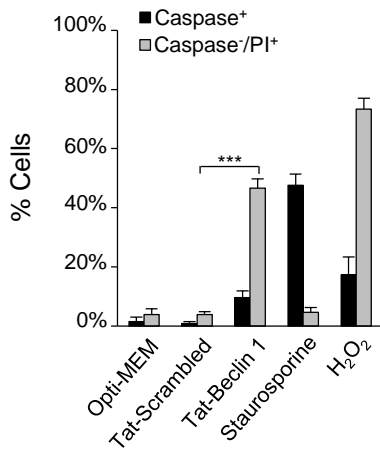
B



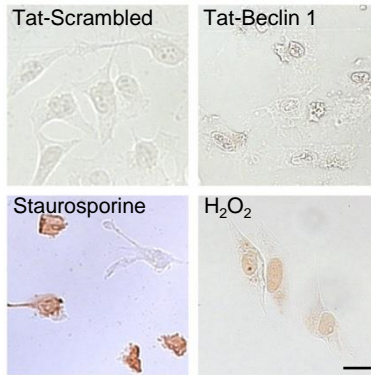
C



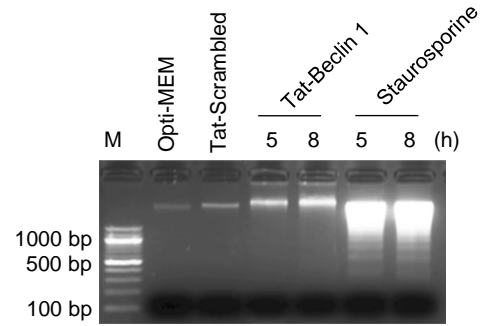
D



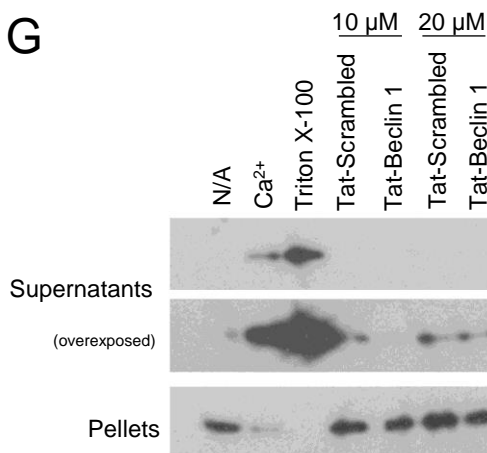
E



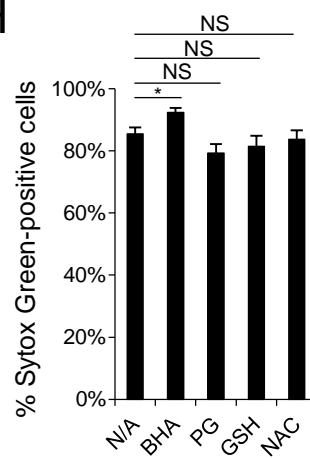
F



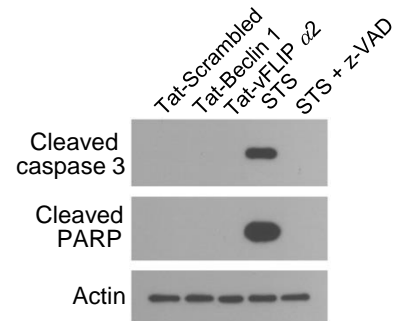
G

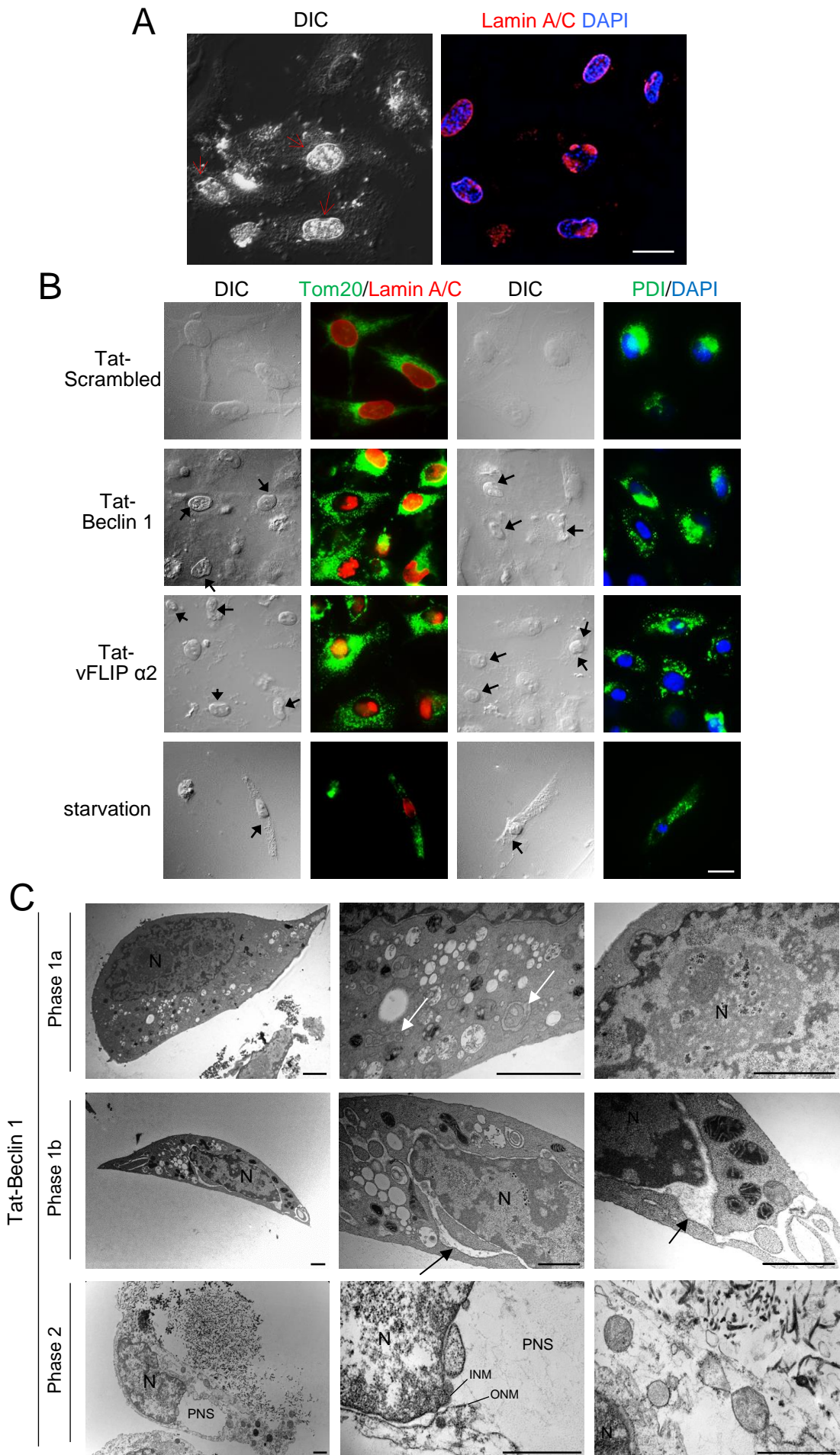


H

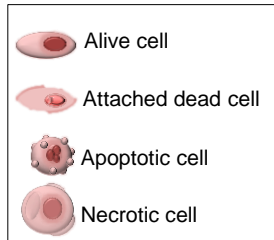
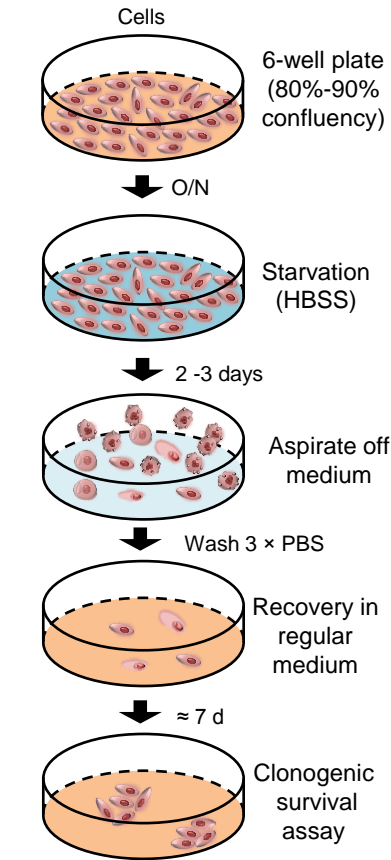


I

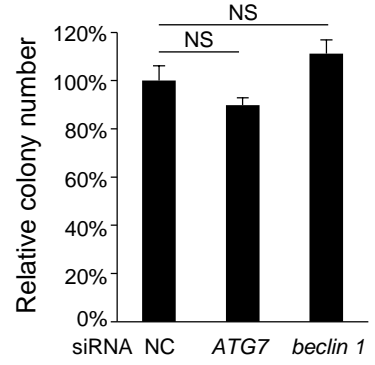
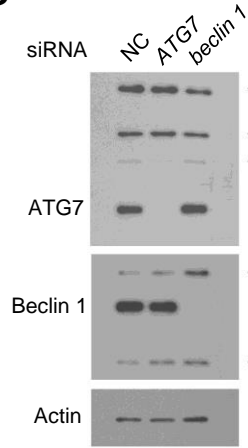




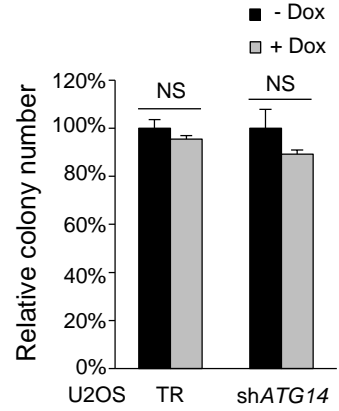
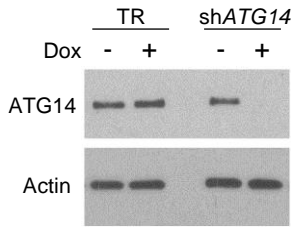
A



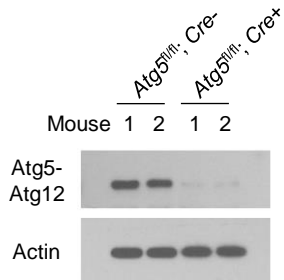
B



C



D



E

